Local Chern Number for Noninteracting Fermions in the Harper-Hofstadter Model

Urs Gebert

Bachelor's Thesis in the Department of Theoretical Physics
at the
Johann Wolfgang Goethe University of Frankfurt

September 21, 2018

Referee: Prof. Dr. W. Hofstetter
Secondary Referee: Prof. Dr. P. Kopietz
Supervisor: B. Irsigler, Prof. Dr. W. Hofstetter

Erklärung nach §30 (12) Ordnung für den Bachelor - und dem Masterstudiengang. Hiermit erkläre ich, dass ich die Arbeit selbstständig und ohne Benutzung anderer als der angegebenen Quellen und Hilfsmittel verfasst habe. Alle Stellen der Arbeit, die wörtlich oder sinngemäß aus Veröffentlichungen oder aus anderen fremden Texten entnommen wurden, sind von mir als solche kenntlich gemacht worden. Ferner erkläre ich, dass die Arbeit nicht - auch nicht auszugsweise - für eine andere Prüfung verwendet wurde.

Frankfurt, den

Contents

1 Introduction

1.1 Content of this Thesis

In this work we will theoretically study noninteracting spinful fermions described by the Harper-Hofstadter Hamiltonian. This Hamiltonian models particles on a square lattice, with a magnetic field perpendicular to the surface coupling to the orbital motion. In section 1.2 we give a short overview on the field of cold atoms experiments, where the Harper-Hofstadter Hamiltonian is experimentally realizable. We will study the phase diagram of this time-reversal invariant Hamiltonian, which has regimes, where the system is in a so-called Quantum Spin Hall (QSH) insulating phase. Such a QSH phase belongs to the field of topological insulators on which we give a brief introduction in section 1.3.
In the physical background section (section 2), we will first discuss the principle of gauge invariance and the Aharonov-Bohm effect to explain how an external magnetic field changes the Hamiltonian of the system. This is needed to understand how neutral atoms, which are used in cold atom experiments, respond to an artifical gauge field in the same way as charged particles to a magnetic field. We also shortly discuss the time-reversal-invariance of the Hamiltonian. Then we will explain the concepts of Berry phase and Berry curvature and derive a formula to calculate the topological invariant, called Chern number, of a set of states. Now we are able to develop our method, the local spin Chern marker, which we are mainly using in this work (section 3). We will derive a real-space formula of the Chern marker from the formula of the Chern number in momentum-space . Afterwards there is a short section on the Bott index, which is another theoretical tool to obtain a topological invariant equivalent to the Chern number of a system. We used this to check some results calculated by the local spin Chern marker. To the Hamiltonian we will add a staggered potential to drive phase transitions and a time-reversal invariant spin-orbit coupling. Using the local spin Chern marker we will first calculate phase diagrams of the topological phases with respect to an increasing staggered potential, with and without spin-orbit coupling (section 4). We also will discuss the influence of different boundary conditions on the phase diagrams, meaning a periodically continued or finite lattice. Afterwards we will add different confining trap potentials to our system and use the local spin Chern marker to obtain the topologically non-trivial regions in this inhomogenous systems, also with and without spin-orbit coupling. In the end we will provide a conclusion of the thesis and a short outlook (section 5).

1.2 Cold Atoms in Optical Lattices

Ultracold quantum gases are dilute clouds of neutral atoms cooled down to temperatures below 10^{-5} Kelvin, where quantum-mechanical properties become important. With the first realization of an atomic Bose-Einstein condensate (BEC), i.e. a system of bosons which all remain in the same single-particle ground state at very low temperatures, in the groups of Ketterle [1] and at the same time Wieman and Cornell [2] this field was made experimentally accessible. Since these experiments there was a rapid development making cold atoms to ideal model systems for probing and simulating quantum physics. The clouds consist typically of fermionic or bosonic alkali atoms, which are cooled down by techniques like laser and evaporative cooling, and have very low densities ($10^{13} - 10^{15}\mathrm{cm}^{-1}$) in comparison to gases at at-

mospheric pressure ($10^{19}\mathrm{cm}^{-1}$), or solids ($10^{22}\mathrm{cm}^{-1}$). These low densities improve the ability to control, manipulate and precisely probe the system. One powerful tool is the possibility to tune interaction strengths between the atoms by Feshbach resonances [3], which for example allowed the study of the BEC to BCS crossover in fermionic cold atoms [4], where the interaction is tuned from attractive to repulsive. By storing cold atoms in optical lattices one has a highly controllable 'quantum simulator' of condensed matter systems. Optical lattices consist of interferring lasers, which create a potential landscape in form of a crystalline lattice. This allows to simulate systems of different lattice geometries and dimensions, with the advantage of having a much smaller system, with regard to particle number, but with larger lattice spacing than in condensed matter systems. The possibilities of adjusting the parameters of these systems are manifold. One example is the quantum transition between superfluid and Mott-insulator in a quantum gas of repulsive bosons [6], which was realized by changing the depth of the lattice or alternatively tuning the interactions [7]. To simulate electrons in a solid in an external magnetic field by cold atoms one has to take into account that there is no coupling between the orbital motion of neutral atoms and the external magnetic field. The solution for this is the engineering of artificial gauge fields to which the atoms respond in the same way as if they experience an orbital magnetic field. There are several approaches of achieving this, such as rotating the lattice [8], shaking the lattice [9] or inducing laser-assisted tunneling [10, 11]. Also spin-orbit coupling could be engineered [12], which completes the set of tools to simulate interesting phenomena of electrons in a solid and even more exotic systems with cold atoms. Interesting is also the study of systems, which are theoretically predicted, but could not be found in real materials. Equally important to the preparation of systems is of course the ability to measure important quantities. Where in typical condensed matter experiments one material sample is prepared and then multiple measurements are taken, until one has enough data, the way of performing measurements in cold atom system is different. After cooling down the sample and preparing it in the prefered way, the lifetime of the experiment is typically very short, since the system heats up very quickly. Also most measurements change or destroy the system, which then has to prepared new for the next measurement. There are several powerful methods available like in-situ imaging [13], time-of-flight imaging and band-mapping [14] to obtain for example momentum distribution, temperature, density, equation of state, correlation functions and other observables of the atom cloud. However, there are also challenges in dealing with such low temperatures and very sensitive systems and therefore one focus of the field is on the search and improvement of methods to prepare and measure those systems.

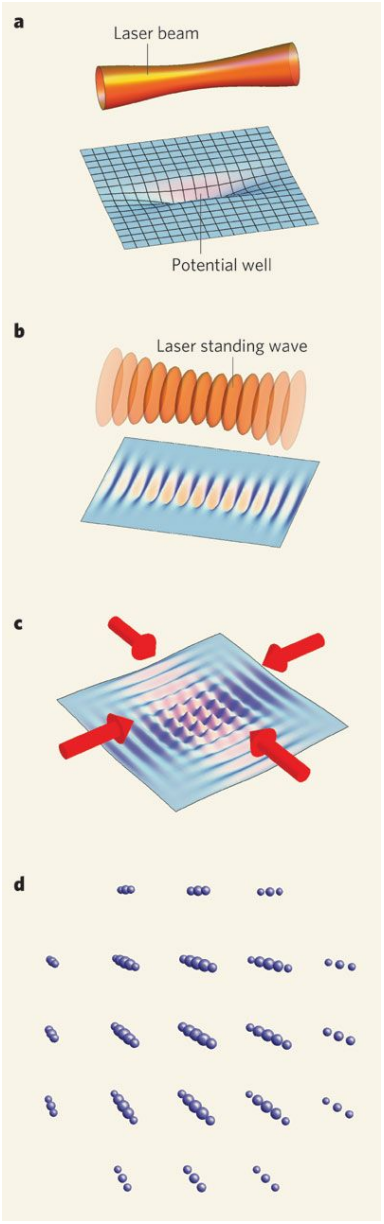

Figure 1: Laser light can create a variety of potential landscapes. Picture taken from [5]

1.3 Topological Insulators

The classical Hall effect describes an electric current in a magnetic field, where due to the Lorentz force, the electrons are displaced perpendicular to the magnetic field and electric current, and induce the so-called Hall voltage. In 1980 von Klitzing et al. [15] disovered a quantized Hall conductivity for a two-dimensional electron gas exposed to a strong magnetic field and at low temperatures. By ramping up the magnetic field, the Hall conductivity changes only at certain strenghts and is fixed in between, resulting in plateaus. This so-called quantum Hall effect could not be explained by the Landau-Ginzburg theory of spontaneous symmetry breaking, which was the current theory to characterize states of matter. The theoretical description given by Laughlin [16] and Thouless [17] provides a quantum Hall state which was topologically different to all states known before. It has a seperated conductance and valence band, just like an insulator, but with gapless states connecting these bands. These states are localized at the edge of the sample and provide dissipationless transport of electric charge. The reason for the appearence of these edge states lies in the topology of the system, and also the Hall conductance is given by a topological invariant. Such topological invariants cannot vary continously, but are quantized and robust against small deformations of the Hamiltonian. A common example for a topological classification is the distinction of closed 2D surfaces by their number of holes. A ball could never be formed into a donut, without breaking a hole in it. Here the number of holes in the surface is a topological invariant. The Gauss-Bonnet theorem gives a formula to calculate this invariant by integrating the curvature over the whole surface. In the same way the topological invariant, classifying a quantum Hall state, could be obtained by an integral over a curvature. The classification of quantum states by their topology gave rise to the new field of topological band theory, including topological insulaters and superconducters, and the search for new materials in which these phenomena occur. In 2005 Kane and Mele [18] and later Bernevig and Zang [19] predicted a Quantum Spin Hall (QSH) state in 2D, which preserves time-reversal symmetry, in contradiction to the Quantum Hall (QH) state, and is induced by spin-orbit coupling. This state is insulating in the bulk, but has counterpropagating spin currents at the edges, with a quantized spin Hall conductance. It was first experimentally observed in 2007 by

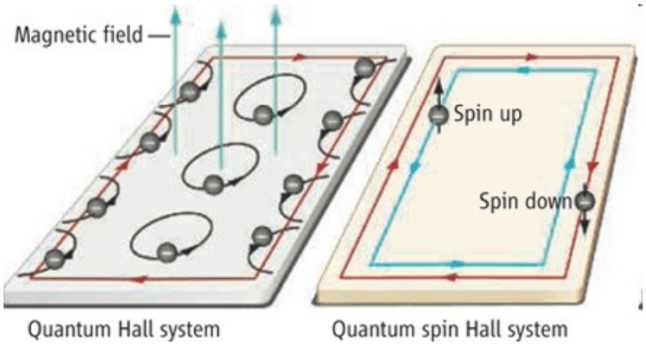

Figure 2: In a quantum Hall system the external magnetic field causes a netflow of charge along the edge. In a QSH system there is no netflow of charge, but counterpropagating spin currents at the edge. Picture taken from [20].

König et al. [21] in HgTe quantum wells. However, it should be possible to observe the QSH effect using cold atoms in optical lattices with their high flexibility. Indeed the time-reversal invariant Harper-Hofstadter Hamiltonian, were a QSH regime is predicted, had been realized in 2013 in the groups of Bloch [11] and Ketterle [22], which shows the important role of cold atom

experiments in engineering model Hamiltonians beyond the possibilities of condensed matter systems. Recent interests include the realization of strongly correlated topological phases with cold atoms to observe for example fractional quantum Hall states.

2 Physical Background

2.1 Gauge Invariance

Artificial gauge fields play an important role in cold atom setups to simulate a magnetic field for neutral atoms. The idea behind them is the engineering of an effective gauge potential similar to the vector potential of a magnetic field. This is possible because in the mathematical description of physical field theories there is often some freedom in choosing certain properties of the underlying potential without changing the physics of the system. For example consider a static magnetic field $\mathbf{B}$ in z-direction. As we know from Maxwell's equations this is divergence free und thus can be written in terms of a vectorpotential $\mathbf{A}$:

$$\mathbf{B} = \nabla \times \mathbf{A}. \tag{2.1}$$

The choice of $\mathbf{A}$ is not unique as we can add the gradient of an arbitrary scalar function χ without changing the magnetic field and therefore without changing the physics of the system:

$$\mathbf{B} = \nabla \times \mathbf{A'} = \nabla \times (\mathbf{A} + \nabla\chi) = \mathbf{B}. \tag{2.2}$$

Adding such a term is called a gauge transformation and the magnetic field is invariant under this gauge transformation. One important gauge we will use in this work is the so-called Landau gauge

$$\mathbf{A} = \begin{pmatrix} 0 \\ B \cdot x \\ 0 \end{pmatrix} \tag{2.3}$$

which describes a magnetic field in z-direction.

$$\mathbf{B} = \nabla \times \begin{pmatrix} 0 \\ B \cdot x \\ 0 \end{pmatrix} = \begin{pmatrix} 0 \\ 0 \\ B \end{pmatrix}. \tag{2.4}$$

A state Ψ in quantum mechanics is gauge invariant under a multipication with a complex phase factor, as it does not change the expectation value of an observable $\hat{O}$.

$$|\Psi\rangle \to e^{i\alpha}|\Psi\rangle \tag{2.5}$$

$$\langle\Psi|\,\hat{O}\,|\Psi\rangle \to \langle\Psi|\,e^{-i\alpha}\hat{O}e^{i\alpha}\,|\Psi\rangle = \langle\Psi|\,\hat{O}\,|\Psi\rangle\,. \tag{2.6}$$

We have even more freedom in the choice of a gauge, since this argument (2.6) is already satisfied by a local gauge transformation

$$|\Psi(\mathbf{r})\rangle \to e^{i\alpha(\mathbf{r})}|\Psi(\mathbf{r})\rangle, \tag{2.7}$$

where $\mathbf{r}$ is a parameter from the parameter space of Ψ.

2.2 Aharonov-Bohm Phase

The question is now what the crucial effect of magnetism experienced by a charged particle is. The Aharonov-Bohm phase is a geometric phase picked up by a particle moving through regions where an external magnetic field is zero, but the respective vector potential is not. It is a measurable quantitiy and shows that the description by fields alone is not enough to describe the physics of a system. Therefore the geometric phase is even something more fundamental and the magnetic field experienced by the particle could be seen as a consequence of the geometric phase. The idea was introduced by Aharonov and Bohm in 1959 in a gedanken experiment [23]. We follow the derivation of a seminar by Kregar [24]. Imagine an ideal solenoid with internal magnetic field $\mathbf{B}$ and zero magnetic field on the outside. So the outside vector potential $\mathbf{A}$ depends on the chosen gauge, but has to fulfill

$$\mathbf{B} = \nabla \times \mathbf{A} = 0, \tag{2.8}$$

and Stokes' theorem

$$\oint_{\mathcal{C}} \mathbf{A} \cdot \mathrm{d}\mathbf{r} = \int_{\mathcal{S}} \mathbf{B} \cdot \mathrm{d}\mathbf{S} = \Phi_m, \tag{2.9}$$

where Φ_m is the magnetic flux through the solenoid if the closed curve $\mathcal{C}$ encircles it. That already shows even if the magnetic field is zero everywhere outside the solenoid, the vector potential cannot be zero. The Hamiltonian for a charged particle in an external magnetic field reads

$$\hat{H} = \frac{1}{2m} \left[i\hbar\nabla + e\mathbf{A}(\mathbf{r}) \right]^2 . \tag{2.10}$$

The dynamics of this particle is described by the Schrödinger equation

$$i\hbar \frac{\partial \Psi}{\partial t} = H\Psi, \tag{2.11}$$

where $\Psi(\mathbf{r}, t) = \Psi$ is the wavefunction of the particle. With (2.10) inserted in (2.11) we get

$$H\Psi = \frac{1}{2m} (i\hbar\nabla + \mathrm{e}\mathbf{A}(\mathbf{r}))^2 \Psi. \tag{2.12}$$

To solve this we use the ansatz

$$\Psi(\mathbf{r}, t) = e^{ig(\mathbf{r})} \Psi'(\mathbf{r}, t), \tag{2.13}$$

where

$$g(\mathbf{r}) \equiv \frac{e}{\hbar} \int_0^{\mathbf{r}} \mathbf{A}(\mathbf{r}') \cdot \mathrm{d}\mathbf{r}' \tag{2.14}$$

is independent of the path of integration since $\mathbf{A}$ is curl free. Applying the gradient on Ψ (2.13) leads to the relation

$$(-i\hbar\nabla - e\mathbf{A})^2 \Psi = -\hbar^2 e^{ig(\mathbf{r})} \nabla^2 \Psi'. \tag{2.15}$$

Inserting in the Schrödinger equation (2.12) and canceling $e^{ig(\mathbf{r})}$ results in a wave equation for Ψ'

$$i\hbar \frac{\partial \Psi'}{\partial t} = -\frac{\hbar^2}{2m} \nabla^2 \Psi'. \tag{2.16}$$

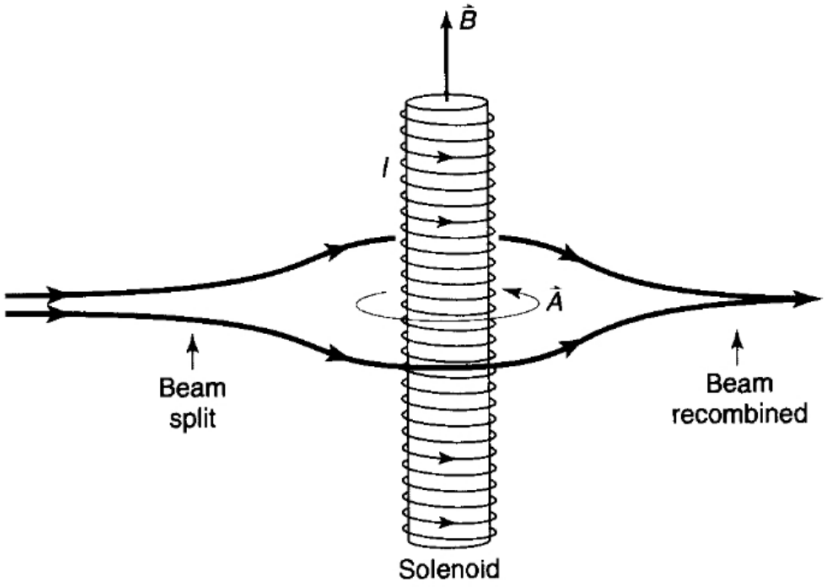

Figure 3: Aharonov-Bohm effect. Two electron beams will acquire a phase difference even if the magnetic field is zero outside the solenoid. Picture taken from [24].

Thus inserting a magnetic field with vector potential A to the Hamiltonian, will change the wave function by multiplying with a phase factor $e^{ig(\mathbf{r})}$.
Two electron beams starting on the same place, travelling right and left towards the solenoid and interferring behind it (figure 27) will acquire a phase difference

$$\Phi_{AB} = g_1 - g_2 = \frac{e}{\hbar}\left[\int_{\mathcal{C}_1} \mathbf{A}(\mathbf{r})\cdot \mathrm{d}\mathbf{r} - \int_{\mathcal{C}_2} \mathbf{A}(\mathbf{r})\cdot \mathrm{d}\mathbf{r}\right] = \frac{e}{\hbar}\oint_{\mathcal{C}} \mathbf{A}(\mathbf{r})\cdot \mathrm{d}\mathbf{r} = \frac{e}{\hbar}\Phi_m, \tag{2.17}$$

which is only caused by the existence of a magnetic field inside the solenoid, although it is zero outside. This is called the magnetic Aharonov-Bohm effect. The acquired phase is gauge invariant, since the integral over the gradient of a scalar function along a closed loop vanishes. Simulating magnetism for neutral atoms is based on the idea of inducing such a geometric phase on neutral atoms.

2.3 Harper-Hofstadter Hamiltonian

In this section we want to discuss the Hamiltonian of the system we are working with. We want to describe fermions in a 2D square lattice. We start with just one particle. Cold atom clouds consist of atoms and not of electrons. However there is a lot of theory describing electrons in crystal lattices, which we use for describing fermionic atoms. As it is standard in condensed matter physics the energy eigenfunctions of a electron in a periodic lattice are described by Bloch waves

$$\Psi(\mathbf{r}) = e^{i\mathbf{k}\cdot\mathbf{r}}u(\mathbf{r}), \tag{2.18}$$

where $u(\mathbf{r})$ has the same periodicity as the lattice. Using Fourier transformation one can construct the so-called Wannier functions which are localized at the sites of the lattice. For an isolated atom the Wannier function would become an atomic orbital, but on a lattice there

is an overlap between the Wannier functions of the nearest sites, so that it is possible for the electron to tunnel from one site to a neighbouring site. Within the tight-binding approximation, where t denotes the tunneling matrix element for tightly bounded electrons, the Hamiltonian of a single electron in a 2D lattice is written in second quantization as

$$\hat{H} = -t \sum_j \left(\hat{a}^\dagger_{j+\hat{x}} \hat{a}_j + \hat{a}^\dagger_{j+\hat{y}} \hat{a}_j + h.c. \right), \tag{2.19}$$

where $j = (x, y)$ denotes the lattice site, $\hat{x}$ and $\hat{y}$ are the unit vectors in x and y direction and $\hat{a}^\dagger_j, \hat{a}_j$ are the creation and annhilation operators of a particle on lattice site j. The terms in the Hamiltonian (2.19) describe hopping between neighbouring lattice sites, which corresponds to the kinetic energy of a tightly bound particle. An electron hopping in an external magnetic field $\mathbf{B} = \nabla \times \mathbf{A}$ in direction $i = \{x, y\}$ will pick up a complex phase $\phi^i_j = -eA^i_j/\hbar$ known as Peierls phase. According to Peierls substitution [25] the Hamiltonian now reads

$$\hat{H} = -t \sum_j \left(e^{i\phi^x_j} \hat{a}^\dagger_{j+\hat{y}} \hat{a}_j + e^{i\phi^y_j} \hat{a}^\dagger_{j+\hat{x}} \hat{a}_j + h.c. \right). \tag{2.20}$$

Going along a closed loop and adding all Peierls phases shows the equivalence to the Aharonov-

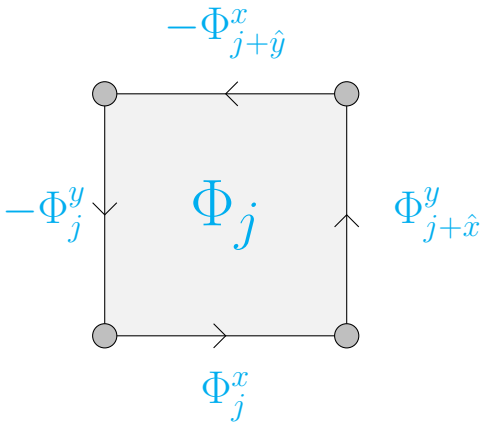

Figure 4: Magnetic flux Φ_j and Peierls phases of one plaquette in a square lattice.

Bohm phase

$$\Phi_{AB} = \frac{e}{\hbar} \oint_C \mathbf{A} \cdot \mathrm{d}\mathbf{r} \tag{2.21}$$

If the magnetic flux is homogenous, it is useful to define the magnetic flux per plaquette

$$\alpha = \frac{\Phi}{2\pi} = \frac{1}{2\pi} \left(\phi^x_j + \phi^y_{j+\hat{x}} - \phi^x_{j+\hat{y}} - \phi^y_j \right). \tag{2.22}$$

Now we can write the Harper-Hofstadter Hamiltonian in the Landau gauge ($\phi^x_j = 0, \phi^y_j = \Phi \cdot x$):

$$\hat{H} = -t \sum_j \left(\hat{a}^\dagger_{j+\hat{x}} \hat{a}_j + e^{i2\pi\alpha x} \hat{a}^\dagger_{j+\hat{y}} \hat{a}_j + h.c. \right) \tag{2.23}$$

As said before we can use this Hamiltonian not only for an electron, but for a fermionic cold atom (or also bosonic atom) which experiences a vector potential $\mathbf{A}$. We want to describe spin-$\frac{1}{2}$

particles so we need to introduce spin in the Hamiltonian. There could be one spin up as well as one spin down on each site which we express in spinors of fermionic creation and annhilation operators,

$$\hat{c}^\dagger = \begin{pmatrix} \hat{c}^\dagger_\uparrow \\ \hat{c}^\dagger_\downarrow \end{pmatrix}, \ \hat{c} = \begin{pmatrix} \hat{c}_\uparrow \\ \hat{c}_\downarrow \end{pmatrix}. \tag{2.24}$$

In this work we want to specifically look at time-reversal invariant systems. The anti-unitary time-reversal operator $\hat{\mathcal{T}} : t \to -t$ changes the sign of the linear momentum $\mathbf{k}$ and angular momentum of a particle. Since the spin s of a particle is an angular momentum, it will be flipped by the time-reversal operator.

$$\hat{\mathcal{T}} \left|\mathbf{k}, s\right\rangle = \eta \left|-\mathbf{k}, -s\right\rangle, \tag{2.25}$$

where η could be an arbitrary phase. To get time-reversal symmetry the Hamiltonian has to commute with the time-reversal operator

$$\hat{\mathcal{T}}\hat{H} \left|\mathbf{k}, s\right\rangle = \hat{H}\hat{\mathcal{T}} \left|\mathbf{k}, s\right\rangle. \tag{2.26}$$

In our system hopping in one direction induces a complex phase conjugate to the phase from hopping in opposite direction. To get time-reversal invariance this phase has to have different signs for spin up and down particles. If one inverts now the direction of hopping and the spin of a particle it picks up the same phase as before, and therefore leaves the Hamiltonian invariant. Mathematically this is reached by inserting a σ_z Pauli matrix in the phase.

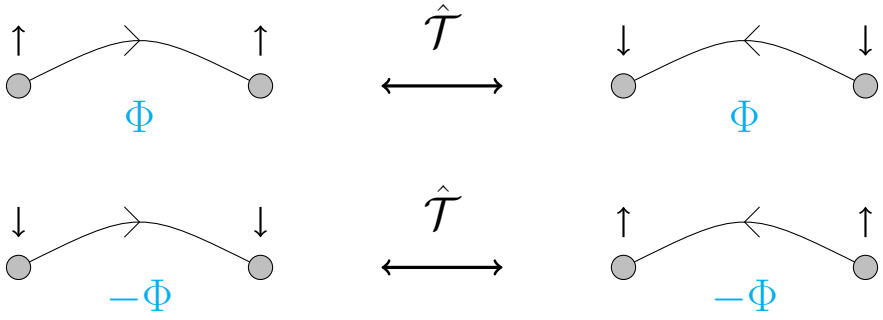

Figure 5: Time-reversal inverts direction of hopping and spin. Hopping is time-reversal invariant, if the induced phase has different signs for spin up and spin down.

$$\hat{H} = -t \sum_j \left(\hat{c}^\dagger_{j+\hat{x}} \hat{c}_j + \hat{c}^\dagger_{j+\hat{y}} e^{i2\pi\alpha x \sigma_z} \hat{c}_j + h.c. \right). \tag{2.27}$$

Expanding the e-function results in a conjugate contribution to the second component of the spinors and therefore a different sign of the phase for spin up and spin down.

$$e^{ix\sigma_z} = \mathbb{1} \cdot \cos(x) + i\sigma_z \cdot \sin(x) = \begin{pmatrix} e^{ix} & 0 \\ 0 & e^{-ix} \end{pmatrix} \tag{2.28}$$

In a spin-1/2 system time-reversal symmetry yields an interesting consequence known as Kramers degeneracy [26]. Here the squared time-reversal operator yields a negative identity,

$$\hat{\mathcal{T}}^2 = -\mathbb{1}. \tag{2.29}$$

$|E\rangle$ and $\hat{\mathcal{T}}|E\rangle$ have the same energy eigenvalue, since $\hat{\mathcal{T}}$ commutes with the Hamiltonian. If we assume

$$\hat{\mathcal{T}}|E\rangle = \eta|E\rangle\,, \tag{2.30}$$

this contradicts (2.29), since

$$\hat{\mathcal{T}}^2|E\rangle = |\eta|^2|E\rangle \neq -|E\rangle\,, \tag{2.31}$$

where the absolute value is due to the antiunitarity of $\hat{\mathcal{T}}$. This shows $|E\rangle$ and $\hat{\mathcal{T}}|E\rangle$ have to be two different states with the same energy eigenvalue. Therefore the Hamiltonian is degenerate and for every energy eigenvalue there has to be at least one so-called Kramers pair of degenerate states.

2.4 Berry Phase, Berry Curvature, Chern Number

We discussed geometric phases like Aharonov-Bohm and Peierls phase before and our goal now is to find gauge invariant quantities related to them. In the end of this section we will derive a formula for the important Chern number, which is used to classify the topological order of a system. We will follow the course on topological insulators of J.K. Asbóth [27].
Multiplication of a state with a phase is a gauge transformation in quantum mechanics, as it does not change the expectation value of an observable as described in section 2.1. Therefore physical information is only represented by gauge invariant quantities. Clearly the phase of a state $|\Psi\rangle$ represents no physical information as it could be manipulated by a gauge transformation. The relative phase γ_{12} between nonorthogonal states $|\Psi_1\rangle\,, |\Psi_2\rangle$ determined through

$$e^{-i\gamma_{12}} = \frac{\langle\Psi_1|\Psi_2\rangle}{|\langle\Psi_1|\Psi_2\rangle|}, \qquad \gamma_{12} \in (-\pi, \pi] \tag{2.32}$$

is also not invariant under a local gauge transformation as discussed in section 2.1, since plugging

$$|\Psi\rangle_j \to e^{i\alpha_j}|\Psi\rangle_j \tag{2.33}$$

into equation (2.32) leads to

$$e^{-i\gamma_{12}} \to e^{-i\gamma_{12}+i(\alpha_2-\alpha_1)}, \tag{2.34}$$

which is only invariant if $\alpha_1 = \alpha_2$: One needs at least three states to form a loop on which the phases are added (see figure 6a).

$$\gamma_L = -\arg\, e^{-i(\gamma_{12}+\gamma_{23}+\gamma_{31})} = -\arg(\langle\Psi_1|\Psi_2\rangle\langle\Psi_2|\Psi_3\rangle\langle\Psi_3|\Psi_1\rangle) \tag{2.35}$$

The function $\arg(x)$ maps the complex phase of x between $-\pi$ and π. One can rewrite the term above as

$$\gamma_L = -\arg\, \mathrm{Tr}(|\Psi\rangle_1\langle\Psi_1|\Psi_2\rangle\langle\Psi_2|\Psi_3\rangle\langle\Psi_3|) \tag{2.36}$$

to get the so-called Berry phase γ_L as an expression of gauge invariant projectors $|\Psi_i\rangle\langle\Psi_i|$. The Berry phase is gauge invariant, since it depends on gauge invariant projectors, and is of course defined for an arbitrary number (greater than two) of nonorthogonal states ordered in a loop. One could see the similarities with the Aharonov-Bohm phase as we now go to quantum states

ordered in a finite two dimensional square lattice. The Berry phase around one plaquette with index mn consisting here of four sites is called Berry flux F_{mn} through plaquette mn,

$$F_{mn} = -\arg \exp[-i(\gamma_{(m,n),(m+1,n)} + \gamma_{(m+1,n),(m+1,n+1)} - \gamma_{(m,n+1),(m+1,n+1)} - \gamma_{(m,n),(m,n+1)})]. \tag{2.37}$$

Adding the Berry flux of neighbouring plaquettes will cancel the inner edges i.e. the common edge of two plaquettes as shown in figure 6b. The connection to the Berry phase of a greater

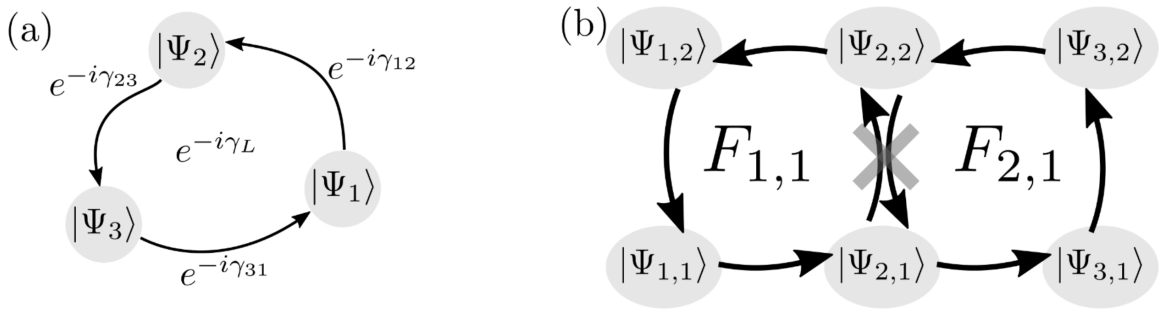

Figure 6: Berry phase γ_L and Berry flux $F_{m,n}$. Picture taken from [27].

loop is given by

$$\exp\left[-i\sum_m\sum_n F_{mn}\right] = e^{-i\gamma_L}, \tag{2.38}$$

where the sum is over all plaquettes inside the loop. The equality of the total Berry flux and Berry phase only holds up to modulo of 2π.
Now we look at a closed surface. Here all edges are inner edges canceling each other and therefore

$$\exp\left[-i\sum_{mn} F_{mn}\right] = 1. \tag{2.39}$$

However the Chern number

$$Q = \frac{1}{2\pi}\sum_{mn} F_{mn} \tag{2.40}$$

does not have to be zero, but is an integer.
We now want to go from the discrete to the continuum case. The analogon to the relative phase (2.32) is given by

$$e^{-i\Delta\gamma} = \frac{\langle\Psi(\mathbf{r})|\Psi(\mathbf{r}+\mathrm{d}\mathbf{r})\rangle}{|\langle\Psi(\mathbf{r})|\Psi(\mathbf{r}+\mathrm{d}\mathbf{r})\rangle|}, \tag{2.41}$$

where $\mathbf{r}$ is some parameter in parameterspace of Ψ, not necessarily a position vector. For $\mathrm{d}\mathbf{r} \to 0$ one finds

$$\Delta\gamma = i\langle\Psi(\mathbf{r})|\nabla_r|\Psi(\mathbf{r})\rangle \cdot \mathrm{d}\mathbf{r} = \mathbf{A}\cdot\mathrm{d}\mathbf{r}, \tag{2.42}$$

where $\mathbf{A}$ is called Berry connection. $\mathbf{A}$ is not gauge invariant like the relative phase, but we can now define the gauge invariant Berry phase along a closed curve $\mathcal{C}$ going from the discrete(2.36) to the continuum case:

$$\gamma_{\mathcal{C}} = -\arg \exp\left[-i \oint_{\mathcal{C}} \mathbf{A} \cdot \mathrm{d}\mathbf{r}\right] \tag{2.43}$$

To find the quantity corresponding to the Berry flux we go to the limit of an infinitly fine grid with steps $\Delta x, \Delta y \to 0$. One could always find a gauge $|\Psi\rangle \to |\Psi'\rangle, \mathbf{A} \to \mathbf{A}'$ in the way that $|\Psi'\rangle, \mathbf{A}'$ are smooth in the plaquette mn.

$$\begin{aligned} F'_{mn} =& A'_x(x_m + \frac{\Delta x}{2}, y_n)\Delta x + A'_y(x_{m+1}, y_n + \frac{\Delta y}{2})\Delta y \\ & - A'_x(x_m + \frac{\Delta x}{2}, y_{n+1})\Delta x - A'_y(x_m, y_n + \frac{\Delta y}{2})\Delta y \\ =& [\partial_x A'_y - \partial y A'_x]\Delta x \Delta y \end{aligned} \tag{2.44}$$

We can now define the Berry curvature B as the Berry flux through an infinitesimal small area $\Delta_x \Delta_y$

$$B = \lim_{\Delta x, \Delta_y \to 0} \frac{F'_{mn}}{\Delta x \Delta y} = \partial_x A'_y - \partial y A'_x, \tag{2.45}$$

and find the relation

$$\exp\left[-i \oint_{\mathcal{C}} \mathbf{A} \cdot \mathrm{d}\mathbf{r}\right] = \exp\left[-i \int_{\mathcal{S}} B(x,y)\mathrm{d}x\mathrm{d}y\right], \tag{2.46}$$

where the right hand side integration is over the surface $\mathcal{S}$ inside the curve $\mathcal{C}$. If one integrates over a closed surface $\mathcal{S}$ all inner edges are canceling, like in the discrete case in figure 6b, and one gets a multiple of 2π, which yields a definition of the Chern number similar to (2.40):

$$Q = \frac{1}{2\pi} \int_{\mathcal{S}} B(x,y)\mathrm{d}x\mathrm{d}y \tag{2.47}$$

3 Methods

3.1 Local Chern Marker in a 2D Lattice

In this chapter we want to develop a method to calculate a local Chern marker of particles in a 2D lattice in real-space. The energy band structure of such systems can be computed from the momentum-space Hamiltonian using the Schrödinger equation

$$\hat{H}(\mathbf{k}) |\Psi_n(\mathbf{k})\rangle = E_n(\mathbf{k}) |\Psi_n(\mathbf{k})\rangle . \tag{3.1}$$

The system is periodic and thus can be expressed in Bloch orbitals

$$\Psi_{n\mathbf{k}}(\mathbf{r}) = e^{i\mathbf{k}\cdot\mathbf{r}} u_{n\mathbf{k}}(\mathbf{r}). \tag{3.2}$$

The $u_{n\mathbf{k}}$ are the periodic parts of the Bloch orbitals, normalized with respect to the unit cell area A_c.

$$\int_{A_c} \mathrm{d}\mathbf{r}\ u^*_{n\mathbf{k}}(\mathbf{r}) u_{n'\mathbf{k}}(\mathbf{r}) = \delta_{nn'}. \tag{3.3}$$

The $u_{n\mathbf{k}}$ are periodic in the first Brillouin zone BZ, which corresponds to a closed surface in k-space. So we can calculate a Chern number $Q^{(n)}$ for the n-th band by integrating the Berry curvature over the first Brillouin zone. The Berry connection of the n-th band is

$$A_{nj} = i \langle u_{n\mathbf{k}} | \partial_{k_j} | u_{n\mathbf{k}} \rangle , \qquad j = x, y. \tag{3.4}$$

From that we get an expression for the Berry curvature (2.45):

$$B(k_x, k_y) = \frac{\partial A_{ny}}{\partial k_x} - \frac{\partial A_{nx}}{\partial k_y} = -2\mathrm{Im} \left\langle \frac{\partial u_{n\mathbf{k}}}{\partial k_x} | \frac{\partial u_{n\mathbf{k}}}{\partial k_y} \right\rangle \tag{3.5}$$

To calculate the total Chern number C of the system we have to sum up the Chern numbers of all occupied bands,

$$C = \sum_{n=1}^{N_c} Q^{(n)} = -\frac{1}{\pi} \mathrm{Im} \sum_{n=1}^{N_c} \int_{BZ} \mathrm{d}\mathbf{k} \left\langle \frac{\partial u_{n\mathbf{k}}}{\partial k_x} | \frac{\partial u_{n\mathbf{k}}}{\partial k_y} \right\rangle , \tag{3.6}$$

where N_c is the lable of the highest filled band. The formula (3.6) is the standard expression for the Chern number on a periodic lattice, where we have well defined quasi-momentum $\mathbf{k}$. For lattices with open boundary conditions (OBC) it would be useful to have an expression in coordinate space. We will follow the derivation of Bianco and Resta [28] and Tran et al. [29] to obtain this. By inserting a complete set of states we get

$$C = -\frac{1}{\pi} \mathrm{Im} \sum_{n=1}^{N_c} \sum_{n'=1}^{\infty} \int_{BZ} \mathrm{d}\mathbf{k} \left\langle \frac{\partial u_{n\mathbf{k}}}{\partial k_x} | u_{n'\mathbf{k}} \right\rangle \left\langle u_{n'\mathbf{k}} | \frac{\partial u_{n\mathbf{k}}}{\partial k_y} \right\rangle . \tag{3.7}$$

We now use

$$\frac{\partial}{\partial k_j} \langle u_{n\mathbf{k}} | u_{n'\mathbf{k}} \rangle = 0, \qquad j = x, y \tag{3.8}$$

$$\Leftrightarrow \qquad \left\langle \frac{\partial u_{n\mathbf{k}}}{\partial k_j} | u_{n'\mathbf{k}} \right\rangle = - \left\langle u_{n\mathbf{k}} | \frac{\partial u_{n'\mathbf{k}}}{\partial k_j} \right\rangle , \tag{3.9}$$

to evaluate the argument of the integral. For the terms in the double sum in (3.7) with $n' = n$ we find

$$\begin{aligned} &\left\langle \frac{\partial u_{n\mathbf{k}}}{\partial k_x} | u_{n\mathbf{k}} \right\rangle \left\langle u_{n\mathbf{k}} | \frac{\partial u_{n\mathbf{k}}}{\partial k_y} \right\rangle \\ =&\left\langle u_{n\mathbf{k}} | \frac{\partial u_{n\mathbf{k}}}{\partial k_x} \right\rangle \left\langle \frac{\partial u_{n\mathbf{k}}}{\partial k_y} | u_{n\mathbf{k}} \right\rangle \\ =&\left(\left\langle \frac{\partial u_{n\mathbf{k}}}{\partial k_x} | u_{n\mathbf{k}} \right\rangle \left\langle u_{n\mathbf{k}} | \frac{\partial u_{n\mathbf{k}}}{\partial k_y} \right\rangle \right)^* , \end{aligned} \tag{3.10}$$

therefore the imaginary part of these products has to be zero. Now consider two different labels $n_1 \neq n_2$. We find

$$\begin{aligned} &\mathrm{Im} \left(\left\langle \frac{\partial u_{n_1\mathbf{k}}}{\partial k_x} | u_{n_2\mathbf{k}} \right\rangle \left\langle u_{n_2\mathbf{k}} | \frac{\partial u_{n_1\mathbf{k}}}{\partial k_y} \right\rangle + \left\langle \frac{\partial u_{n_2\mathbf{k}}}{\partial k_x} | u_{n_1\mathbf{k}} \right\rangle \left\langle u_{n_1\mathbf{k}} | \frac{\partial u_{n_2\mathbf{k}}}{\partial k_y} \right\rangle \right) \\ =&\mathrm{Im} \left(\left\langle \frac{\partial u_{n_1\mathbf{k}}}{\partial k_x} | u_{n_2\mathbf{k}} \right\rangle \left\langle u_{n_2\mathbf{k}} | \frac{\partial u_{n_1\mathbf{k}}}{\partial k_y} \right\rangle + \left\langle u_{n_2\mathbf{k}} | \frac{\partial u_{n_1\mathbf{k}}}{\partial k_x} \right\rangle \left\langle \frac{\partial u_{n_1\mathbf{k}}}{\partial k_y} | u_{n_2\mathbf{k}} \right\rangle \right) \\ =&\mathrm{Im} \left(\left\langle \frac{\partial u_{n_1\mathbf{k}}}{\partial k_x} | u_{n_2\mathbf{k}} \right\rangle \left\langle u_{n_2\mathbf{k}} | \frac{\partial u_{n_1\mathbf{k}}}{\partial k_y} \right\rangle + c.c. \right) \\ =&0. \end{aligned} \tag{3.11}$$

So for every $n = n_1, n' = n_2 \in [1, N_c]$ in the double sum in (3.7), there is one term $n = n_2, n' = n_1$, with wich the imaginary part gets canceled. Therefore we got rid of all terms with $n' \leq N_c$. We can rewrite (3.7):

$$C = -\frac{1}{\pi}\mathrm{Im}\sum_{n=1}^{N_c}\sum_{n'=N_c+1}^{\infty}\int_{BZ}\mathrm{d}\mathbf{k}\left\langle\frac{\partial u_{n\mathbf{k}}}{\partial k_x}|u_{n'\mathbf{k}}\right\rangle\left\langle u_{n'\mathbf{k}}|\frac{\partial u_{n\mathbf{k}}}{\partial k_y}\right\rangle. \tag{3.12}$$

By identifiing the position operator $\hat{\mathbf{r}}$ with its momentum representation

$$\hat{\mathbf{r}} = i\nabla_{\mathbf{k}}, \tag{3.13}$$

we find

$$\langle u_{n'\mathbf{k}}|\nabla_{\mathbf{k}}u_{n\mathbf{k}}\rangle = -i\left\langle\Psi_{n'\mathbf{k}}\right|\hat{\mathbf{r}}\left|\Psi_{n\mathbf{k}}\right\rangle, \qquad n' \neq n, \tag{3.14}$$

These terms are ill-defined for $n' = n$ since the position operator is ill-defined within periodic boundary conditions (PBC) of the form $\Psi(\mathbf{r}) = \Psi(\mathbf{r}+\mathbf{R})$. The off-diagonal terms are well defined as long as the Hamiltonian is noninteracting as following consideration shows [30]. A single-particle Hamiltonian could be written in terms of free kinetic energy and an effective potential $V_{eff}(\mathbf{r}, t)$:

$$\hat{H} = \frac{-\hbar^2}{2m}\nabla_{\mathbf{r}}^2 + \hat{V}_{eff}(\mathbf{r}, t) \tag{3.15}$$

$$\hat{H}\left|\Psi_{n\mathbf{k}}\right\rangle = E_{n\mathbf{k}}\left|\Psi_{n\mathbf{k}}\right\rangle \tag{3.16}$$

Because of

$$\left\langle\Psi_{n'\mathbf{k}}\right|\left[\hat{H}, \hat{\mathbf{r}}\right]\left|\Psi_{n\mathbf{k}}\right\rangle = \left(E_{n'\mathbf{k}} - E_{n\mathbf{k}}\right)\left\langle\Psi_{n'\mathbf{k}}\right|\hat{\mathbf{r}}\left|\Psi_{n\mathbf{k}}\right\rangle, \tag{3.17}$$

we can now replace the position operator in (3.14) by its commutator with the Hamiltonian $\hat{H}$

$$\left\langle\Psi_{n'\mathbf{k}}\right|\hat{\mathbf{r}}\left|\Psi_{n\mathbf{k}}\right\rangle = \frac{\left\langle\Psi_{n'\mathbf{k}}\right|\left[\hat{H}, \hat{\mathbf{r}}\right]\left|\Psi_{n\mathbf{k}}\right\rangle}{E_{n'\mathbf{k}} - E_{n\mathbf{k}}}, \qquad n' \neq n, \tag{3.18}$$

where the commutator gives

$$[\hat{H}, \hat{\mathbf{r}}] = \frac{-\hbar^2}{m}\nabla_{\mathbf{r}} + [V_{eff}, \mathbf{r}] = \frac{-i\hbar^2\mathbf{k}}{m} + [V_{eff}, \mathbf{r}]. \tag{3.19}$$

As long as the effective Potential V_{eff} is local, equation (3.19) depends only on the momentum operator, which is well-defined within PBC. Therefore the off-diagonal matrix elements in (3.18), respectively (3.14) are also well defined. We can rewrite the formula for the Chern number (3.12)

$$C = -\frac{1}{\pi}\mathrm{Im}\sum_{n=1}^{N_c}\sum_{n'=N_c+1}^{\infty}\int_{BZ}\mathrm{d}\mathbf{k}\left\langle\Psi_{n\mathbf{k}}\right|\hat{x}\left|\Psi_{n'\mathbf{k}}\right\rangle\left\langle\Psi_{n'\mathbf{k}}\right|\hat{y}\left|\Psi_{n\mathbf{k}}\right\rangle, \tag{3.20}$$

and insert a complete set of states

$$\mathbb{1} = \frac{A_c}{(2\pi)^2}\sum_{n=1}^{\infty}\int_{BZ}\mathrm{d}\mathbf{k}\left|\Psi_{n\mathbf{k}}\right\rangle\left\langle\Psi_{n\mathbf{k}}\right|, \tag{3.21}$$

where A_c is the area of the unit cell. We find

$$\begin{aligned}
C &= -\frac{1}{\pi}\frac{A_c}{(2\pi)^2}\mathrm{Im}\sum_{n=1}^{N_c}\sum_{n'=N_c+1}^{\infty}\sum_{n''=1}^{\infty}\int_{BZ}\mathrm{d}\mathbf{k}\int_{BZ}\mathrm{d}\mathbf{k}'\,\langle\Psi_{n\mathbf{k}}|\,\hat{x}\,|\Psi_{n''\mathbf{k}'}\rangle\,\langle\Psi_{n''\mathbf{k}'}|\Psi_{n'\mathbf{k}}\rangle\,\langle\Psi_{n'\mathbf{k}}|\,\hat{y}\,|\Psi_{n\mathbf{k}}\rangle \\
&= -\frac{1}{\pi}\frac{A_c}{(2\pi)^2}\mathrm{Im}\sum_{n=1}^{N_c}\sum_{n'=N_c+1}^{\infty}\sum_{n''=1}^{\infty}\int_{BZ}\mathrm{d}\mathbf{k}\int_{BZ}\mathrm{d}\mathbf{k}'\,\langle\Psi_{n\mathbf{k}}|\,\hat{x}\,|\Psi_{n''\mathbf{k}'}\rangle\,\delta_{n''n'}\delta(\mathbf{k}'-\mathbf{k})\,\langle\Psi_{n'\mathbf{k}}|\,\hat{y}\,|\Psi_{n\mathbf{k}}\rangle \\
&= -\frac{1}{\pi}\frac{A_c}{(2\pi)^2}\mathrm{Im}\sum_{n=1}^{N_c}\sum_{n'=N_c+1}^{\infty}\int_{BZ}\mathrm{d}\mathbf{k}\int_{BZ}\mathrm{d}\mathbf{k}'\,\langle\Psi_{n\mathbf{k}}|\,\hat{x}\,|\Psi_{n'\mathbf{k}'}\rangle\,\langle\Psi_{n'\mathbf{k}'}|\,\hat{y}\,|\Psi_{n\mathbf{k}}\rangle\,, \qquad (3.22)
\end{aligned}$$

Where $\delta(\mathbf{k})$ is normalized on the first Brillouin-zone

$$\frac{A_c}{(2\pi)^2}\int_{BZ}\mathrm{d}\mathbf{k}\;\delta(\mathbf{k})=1, \qquad (3.23)$$

which yields

$$\frac{A_c}{(2\pi)^2}\sum_{n''=1}^{\infty}\int_{BZ}\mathrm{d}\mathbf{k}''\,\langle\Psi_{n''\mathbf{k}''}|\Psi_{n\mathbf{k}}\rangle=1. \qquad (3.24)$$

Third line of equation (3.22) holds because the matrix elements vanish for $\mathbf{k}\neq\mathbf{k}'$ due to

$$\begin{aligned}
0 &= \nabla_{\mathbf{k}'}\,\langle\Psi_{n\mathbf{k}}|\Psi_{n'\mathbf{k}'}\rangle \\
&= \left(\nabla_{\mathbf{k}'}\,\langle\Psi_{n\mathbf{k}}|\right)|\Psi_{n'\mathbf{k}'}\rangle + \langle\Psi_{n\mathbf{k}}|\left(\nabla_{\mathbf{k}'}\,|\Psi_{n'\mathbf{k}'}\rangle\right) \\
&= \langle\Psi_{n\mathbf{k}}|\left(\nabla_{\mathbf{k}'}\,|\Psi_{n'\mathbf{k}'}\rangle\right) \\
&= -i\,\langle\Psi_{n\mathbf{k}}|\,\hat{\mathbf{r}}\,|\Psi_{n'\mathbf{k}'}\rangle\,. \qquad (3.25)
\end{aligned}$$

If we write (3.22) in terms of a trace over the unit cell, we can identfiy the projection operators onto the occupied and empty states

$$\hat{P}=\frac{A_c}{(2\pi)^2}\sum_{n=1}^{N_c}\int_{BZ}\mathrm{d}\mathbf{k}\,|\Psi_{n\mathbf{k}}\rangle\,\langle\Psi_{n\mathbf{k}}|\,, \qquad (3.26)$$

$$\hat{Q}=\frac{A_c}{(2\pi)^2}\sum_{n=N_c+1}^{\infty}\int_{BZ}\mathrm{d}\mathbf{k}\,|\Psi_{n\mathbf{k}}\rangle\,\langle\Psi_{n\mathbf{k}}|\,, \qquad (3.27)$$

$$\hat{P}+\hat{Q}=\mathbb{1}. \qquad (3.28)$$

Therefore, we insert (3.24) into (3.22), which yields

$$\begin{aligned}
C &= -\frac{1}{\pi}\left(\frac{A_c}{(2\pi)^2}\right)^2\mathrm{Im}\sum_{n''=1}^{\infty}\sum_{n=1}^{N_c}\sum_{n'=N_c+1}^{\infty}\int_{BZ}\mathrm{d}\mathbf{k}''\int_{BZ}\mathrm{d}\mathbf{k}\int_{BZ}\mathrm{d}\mathbf{k}' \\
&\qquad\cdot\,\langle\Psi_{n''\mathbf{k}''}|\Psi_{n\mathbf{k}}\rangle\,\langle\Psi_{n\mathbf{k}}|\,\hat{x}\,|\Psi_{n'\mathbf{k}'}\rangle\,\langle\Psi_{n'\mathbf{k}'}|\,\hat{y}\,|\Psi_{n\mathbf{k}}\rangle \\
&= -\frac{1}{\pi}\mathrm{Im}\sum_{n''=1}^{\infty}\int_{BZ}\mathrm{d}\mathbf{k}''\,\langle\Psi_{n''\mathbf{k}''}|\,\hat{P}\hat{x}\hat{Q}\hat{y}\,|\Psi_{n''\mathbf{k}''}\rangle \\
&= -\frac{1}{\pi}\frac{(2\pi)^2}{A_c}\mathrm{Im}\;\mathrm{Tr}_{\mathrm{cell}}\left(\hat{P}\hat{x}\hat{Q}\hat{y}\right) \\
&= \frac{4\pi}{A_c}\mathrm{Im}\;\mathrm{Tr}_{\mathrm{cell}}\left(\hat{P}\hat{x}\hat{P}\hat{y}\right) \\
&= \frac{1}{A_c}\mathrm{Tr}_{\mathrm{cell}}\left(\hat{\mathfrak{C}}\right). \qquad (3.29)
\end{aligned}$$

The fourth line of (3.29) holds because of

$$[\hat{x}, \hat{y}] = 0, \tag{3.30}$$

and therefore

$$\langle \Psi_{n\mathbf{k}} | \, \hat{x}\hat{y} \, | \Psi_{n\mathbf{k}} \rangle = \left(\langle \Psi_{n\mathbf{k}} | \, \hat{x}\hat{y} \, | \Psi_{n\mathbf{k}} \rangle \right)^* , \tag{3.31}$$

which causes

$$\begin{aligned} & \text{Im Tr}_{\text{cell}} \left(\hat{P}\hat{x}\hat{y} \right) \\ =& \left(\frac{A_c}{(2\pi)^2} \right)^2 \text{Im} \sum_{n=1}^{\infty} \sum_{n'=1}^{Nc} \int_{BZ} \mathrm{d}\mathbf{k} \int_{BZ} \mathrm{d}\mathbf{k}' \, \langle \Psi_{n\mathbf{k}} | \Psi_{n'\mathbf{k}'} \rangle \, \langle \Psi_{n'\mathbf{k}'} | \, \hat{x}\hat{y} \, | \Psi_{n\mathbf{k}} \rangle \\ =& \left(\frac{A_c}{(2\pi)^2} \right)^2 \text{Im} \sum_{n'=1}^{Nc} \int_{BZ} \mathrm{d}\mathbf{k}' \, \langle \Psi_{n'\mathbf{k}'} | \, \hat{x}\hat{y} \, | \Psi_{n'\mathbf{k}'} \rangle \\ =& 0. \end{aligned} \tag{3.32}$$

The formula for the Chern number (3.29) becomes a trace over a unit cell of the real-space Chern marker operator:

$$\hat{\mathfrak{C}} = 4\pi \cdot \text{Im} \left(\hat{P}\hat{x}\hat{P}\hat{y} \right) \tag{3.33}$$

If we evaluate the trace over a unit cell in position basis we find the local Chern number

$$C = \frac{1}{A_c} \int_{\text{cell}} \mathrm{d}\mathbf{r}' \mathfrak{C}(\mathbf{r}'), \tag{3.34}$$

with the local Chern marker

$$\mathfrak{C}(\mathbf{r}) = \langle \mathbf{r} | \, \hat{\mathfrak{C}} \, | \mathbf{r} \rangle . \tag{3.35}$$

We are not only interested in unit cells, but want to obtain the expectation value of the Chern marker operator (3.33) in a greater supercell or even the whole lattice. Within PBC the local Chern number (3.34) is equal for every unit cell and we get for a supercell of area A

$$\langle \hat{\mathfrak{C}} \rangle = \frac{1}{A} \int_{\text{supercell}} \mathrm{d}\mathbf{r}' \mathfrak{C}(\mathbf{r}') = \frac{1}{A_c} \int_{\text{cell}} \mathrm{d}\mathbf{r}' \mathfrak{C}(\mathbf{r}'). \tag{3.36}$$

This is right, if we would have a well defined position operator over the whole lattice. On the other hand we can look at the trace of the local Chern marker operator (3.33) over the whole system

$$\text{Tr}(\hat{\mathfrak{C}}) = 4\pi \cdot \text{Im Tr}(\hat{P}\hat{x}\hat{P}\hat{y}) = -2\pi i \cdot \text{Tr}[\hat{P}\hat{x}\hat{P}, \hat{P}\hat{y}\hat{P}]. \tag{3.37}$$

The trace of a commutator of operators is zero, as long as they are finite dimensional. For OBC it is more intuitive that the global topology should be trivial as it corresponds to a flat manifold. We get

$$\langle \hat{\mathfrak{C}} \rangle = \frac{1}{A} \int_{\text{supercell}} \mathrm{d}\mathbf{r}' \mathfrak{C}(\mathbf{r}') = 0. \tag{3.38}$$

However, the topology of the bulk should not depend on the boundary conditions and we could split into bulk-part and edge-part:

$$0 = \langle \hat{\mathfrak{C}} \rangle = \frac{1}{A} \int_{\text{bulk}} \mathrm{d}\mathbf{r}' \mathfrak{C}(\mathbf{r}') + \frac{1}{A} \int_{\text{edge}} \mathrm{d}\mathbf{r}' \mathfrak{C}(\mathbf{r}') \tag{3.39}$$

$$= \langle \hat{\mathfrak{C}} \rangle_{\text{bulk}} + \langle \hat{\mathfrak{C}} \rangle_{\text{edge}} \tag{3.40}$$

If we cut the edge-part we get an approximate value for the Chern number, which becomes exact in the limit of an infinitly large lattice

$$\langle \hat{\mathfrak{C}} \rangle_{\text{bulk}} \xrightarrow{A \to \infty} C. \tag{3.41}$$

3.2 Bott Index

In this section we want to discuss another method introduced by Loring and Hastings [31] to calculate an integer invariant for the single-particle lattice Hamiltonian $\hat{H}$ defined in equation (2.27). Let $\hat{P}$ be the projector onto the occupied states below the Fermi energy E_F. Due to the tight-binding approximation $\hat{H}$ only describes next neighbour hopping and therefore could be seen as local. Using this one can show that $\hat{P}$ is local whenever E_F is within a gap in the energy spectrum of $\hat{H}$ or even in a mobility gap. A mobility gap is a region in the energy spectrum where all corresponding energy eigenstates are localized. We first parametrize the position of a site (x, y) by angles θ_x and ϕ_y between 0 and 2π. With this we build diagonal matrices Θ and Φ with elements $\Theta_{xx} = \theta_x$ and $\Phi_{yy} = \phi_y$. Using $\hat{P}$ we can now produce band-projected position matrices U and V

$$U = \hat{P}\exp(i\Theta)\hat{P}, \tag{3.42}$$

$$V = \hat{P}\exp(i\Phi)\hat{P}. \tag{3.43}$$

If E_F is in a mobility gap and the system is large, the projector $\hat{P}$ is local and almost commutes with the position matrices $\exp(i\Theta)$ and $\exp(i\Phi)$. Therefore U and V are almost unitary matrices and almost commute with each other

$$UU^\dagger \approx 1, \tag{3.44}$$

$$VV^\dagger \approx 1, \tag{3.45}$$

$$[U, V] \approx 0. \tag{3.46}$$

If one could approximate U and V by a pair of exatly unitary and commuting matrices U' and V' which are close to U and V, then it is possible to find a complete and orthonormal basis of localized Wannier functions spanning the occupied states [32]. The question now is when is this approximation possible. Since U and V are almost unitary and commuting $VUV^\dagger U^\dagger$ is close to the identity. However the complex logarithm

$$\mathrm{tr}(\ln(VUV^\dagger U^\dagger)) = 2\pi i m + r, \tag{3.47}$$

could differ by a multiple of 2π. Here m and r are real and r is close to zero. Using

$$\mathrm{Tr}[\ln(A)] = \ln[\det(A)] \tag{3.48}$$

one finds

$$\det(VUV^\dagger U^\dagger) = \exp(2\pi i m + r), \tag{3.49}$$

where the determinant is real and positive, since $\det(U) = \det(U^\dagger)^*$ and the same for V. Therefore m has to be an integer. Furthermore m is a topological invariant called the Bott index. U and V could only be approximated by exactly commuting matrices if $m = 0$ [33]. For $m \neq 0$ the system is in a topological non trivial phase.

4 Results

4.1 Spinful Noninteracting Fermions in the Hofstadter Model

In the following we study the Hamiltonian of fermions in a 2D square lattice. For the beginning the Hamiltonian reads [34]

$$\hat{H} = -t \sum_j \left(\hat{c}^\dagger_{j+\hat{x}} \hat{c}_j + \hat{c}^\dagger_{j+\hat{y}} e^{i2\pi\alpha x \sigma_z} \hat{c}_j + h.c. \right). \tag{4.1}$$

Here, $j = (x, y)$ indicates the lattice site and $\hat{x} = (1, 0)$ and $\hat{y} = (0, 1)$ are the unit vectors of the square lattice. $\hat{c}^\dagger_j = (\hat{c}^\dagger_{j\uparrow}, \hat{c}^\dagger_{j\downarrow})$ is a spinor of fermions creation operators with up or down spin on lattice site j. The tunneling amplitude t is equal in x and y direction and will be set to 1 for the calculations. σ_z is a Pauli matrix. Hopping in y-direction induces a complex phase, which corresponds to a magnetic field of total flux $\Phi = 2\pi\alpha$ as already discussed in section 2.3. For our calculations we chose $\alpha = 1/6$ and a lattice of 48×48 sites in x and y direction. First we want to look at a system with periodic boundary conditions (PBC). Calculating and diagonalizing this Hamiltonian yields the following plotted dispersion relation in figure 7.

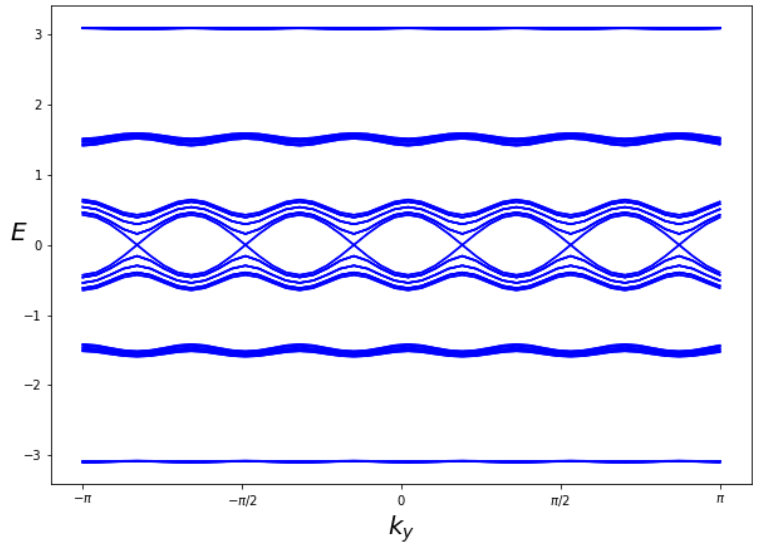

Figure 7: Energy spectrum of a 48×48 square lattice with PBC.

The spectrum splits up to 6 energy bands, due to the chosen $\alpha = 1/6$. The gap between the

energy bands at half filling ($E_F = 0$) is closed, so we obtain a metal phase there. The gaps between the other energy bands are open, which means that the system is insulating within these energies.
PBC correspond to large homogenous systems. Interesting is also the view on systems where there are open boundary conditions (OBC) in at least one direction. This is the case in a cylinder-like geometry, where we have PBC along the surface in y-direction and OBC in x-direction.

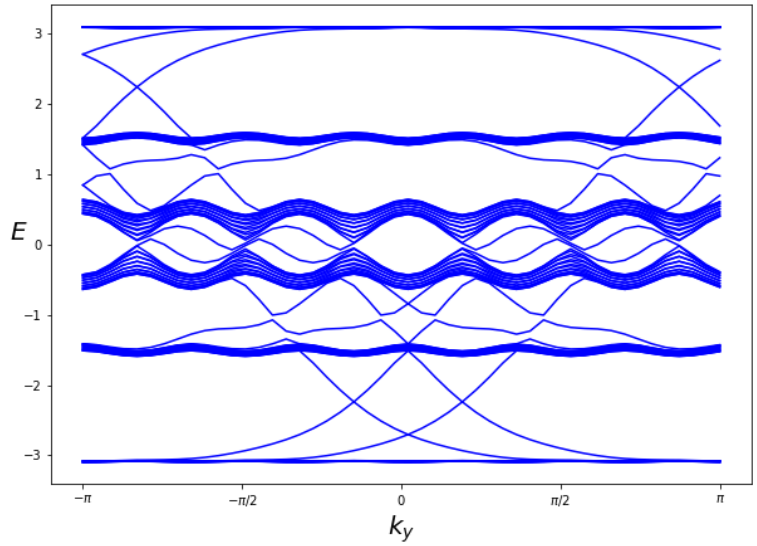

Figure 8: Energy spectrum of a 48×48 square lattice with PBC in y- and OBC in x-direction.

In figure 8 there appear energy bands through the gaps connecting the outer energy bands. Because the system is periodic and therefore translational invariant in y-direction, the momentum in this direction is preserved and the quasi momentum k_y is well defined. The translational invariance in x-direction is broken, so it is interesting to look at the spatial distribution of the wave functions in this direction. Figure 9 shows the same energy spectrum as before, but the points are additionally colored corresponding to the expectation value of their spatial distribution in x-direction

$$\langle x \rangle = \int \Psi(x) x \Psi^*(x) \mathrm{d}x \tag{4.2}$$

and their spin.
In the wide bulk bands, colored in red, there are a lot of overlapping bands with different spins, but the expecation value is everywhere around 24, which is the middle of the lattice. The few energy bands in the gap are located at the edge of the lattice. These states are therefore called edge states, while the other ones are bulk states. We picked one edge and one bulk mode, where the term mode stands for a set of states which are smoothly connected in momentum space [35], to look at the spatial distribution for the same band and different k_y.
The bulk mode is delocalized over the whole system, while the edge mode is on one edge. We now go back to figure 9 and focus on the lowest gap. There are four edge states crossing the gap, two with opposite spin on each edge. We pick for example the blue and the black state. They are located on the same edge but have opposite spin. By looking at $v_y = \frac{\partial E_F}{\partial k_y}$ in the

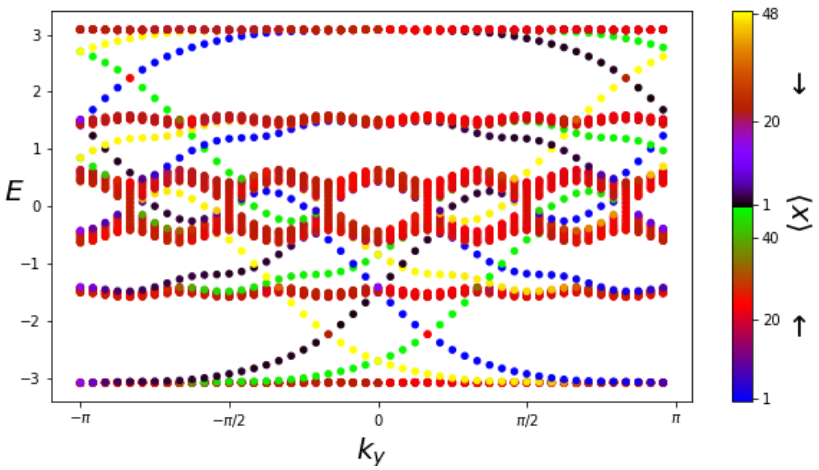

Figure 9: Same energy spectrum as in figure 8 but with colored points corresponding to the spatial expectation value in x-direction.

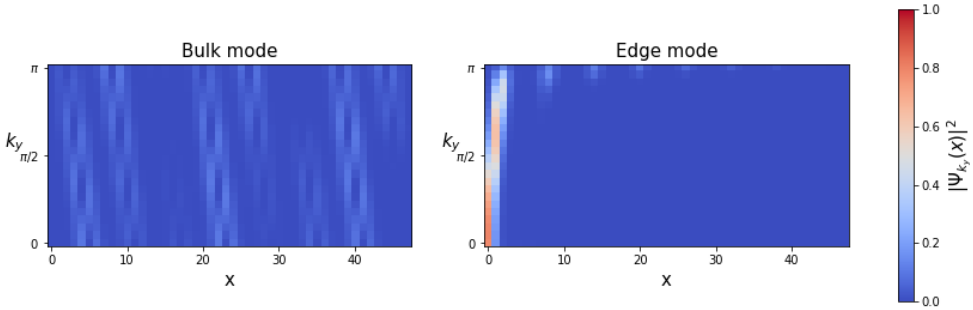

Figure 10: $|\Psi_{k_y}(x)|^2$ as a function of x and k_y for one bulk and one edge mode.

energy spectrum one could obtain the group velocity in y-direction for these bands. The two states which are at the same edge have opposite group velocity. Both, velocity and spin, are changing their sign under time-reversal and therefore the two states together preserve time-reversal symmetry of the Hamiltonian. Such two states have the same energy eigenvalue and form a so-called Kramers pair as discussed in section 2.3 and there is a similar pair on the other edge of the lattice. The two states of a Kramers pair are protected by time-reversal symmetry and can therefore not scatter on each other, nor on the other Kramers pair which is located on the other edge. Since there is no other state to scatter on within the gap, the spin currents are dissipationless. Because both counterpropagating states of a Kramers pair transport the same electric charge, there is no net transport possible. Inside the bulk there are no edge states and no transport of any charge is possible. The system is in a so-called Quantum Spin Hall (QSH) insulator phase. If there are two Kramers pairs on each edge, the pairs could scatter on each other and there are no dissipationless spin currents at the edges. Therefore the system is in a normal insulating phase. In general one could obtain the phase of the system within a gap by counting the Kramers pairs per edge, where an even number means Normal Insulator (NI) and an odd number means QSH insulator. The topological order of the system is given by a $\mathbb{Z}_2$-index [36], which determines the spin Hall conductivity, in contradiction to the electric Hall conductivity in the quantum Hall effect, given by a $\mathbb{Z}$-Chern number. However, the topological order is an attribute of the bulk, while edge modes are an attribute of the boundary conditions. These two are connected by the bulk-boundary-correspondence. Its main statement in time-reversal invariant systems is that the parity of the number of Kramers pairs is equal to the $\mathbb{Z}_2$-index so that $\mathbb{Z}_2$-index of one corresponds to a QSH phase and zero to a normal insulating phase. For our case the lowest and highest gap in figure 9 correspond to a QSH insulating phase, the second highest and lowest to a NI phase, while the gap is closed for $E_F = 0$, which means the system is in a (semi-)metal phase there.
We now want to insert two more terms into the Hamiltonian. First a spin flip term which induces mixing of spin up and down with an amplitude γ when a particle is hopping from one site to the next in x-direction. This term induces Rashba-like spin-orbit coupling [37], which preserves time-reversal symmetry and breaks axial spin symmetry. Secondly an on-site staggered potential in x-direction of strength λ_x. The full Hamiltonian now reads [34]:

$$\hat{H} = -t \sum_j \left[\left(\hat{c}^\dagger_{j+\hat{x}} e^{2\pi i \gamma \sigma_x} \hat{c}_j + \hat{c}^\dagger_{j+\hat{y}} e^{i2\pi\alpha x \sigma_z} \hat{c}_j + h.c. \right) + (-1)^x \lambda_x \hat{c}^\dagger_j \hat{c}_j \right] \tag{4.3}$$

Increasing γ will induce spin mixing, while at $\gamma = 0.25$ the mixing is maximal, in the way that every spin is flipped when hopping in x-direction. To see the effect of the staggered potential we plotted in figure 11 the size of the gap ΔE at half filling ($E_F = 0$) and $\gamma = 0.25$, while increasing λ_x. One can see that increasing the staggered potential first opens the gap then closes it at $\lambda_x \approx 1.2$ and opens it again. By looking at the energy spectra in figure 12 and counting the Kramer's pairs inside the gap at $E_F = 0$ one can see, that there is a QSH phase opening at half filling, while after the gap is closed a NI phase is opening. This is a good example of a topologically protected phase, which could only change by closing a gap in the energy spectrum.

Up to now we only determined the topological phase of the system by counting the Kramers pairs inside the gap. This is not possible in periodic systems, where there are no edges and therefore no edge states. But as mentioned before, the topology is an attribute of the bulk and independent from the boundary conditions; at least if the system is big enough, so that the edge states do not penetrate deep in the bulk.
We will discuss two theoretical tools to obtain the $\mathbb{Z}_2$ invariant of our system from the band

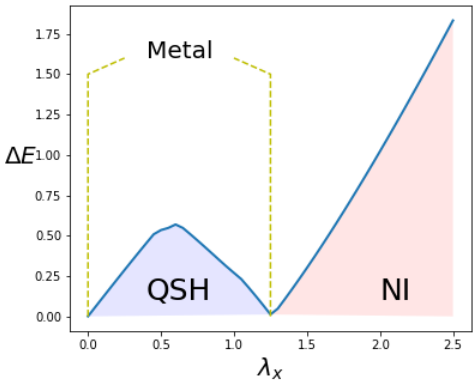

Figure 11: Blue line is the size of the gap at half filling for increasing λ_x and $\gamma = 0.25$.

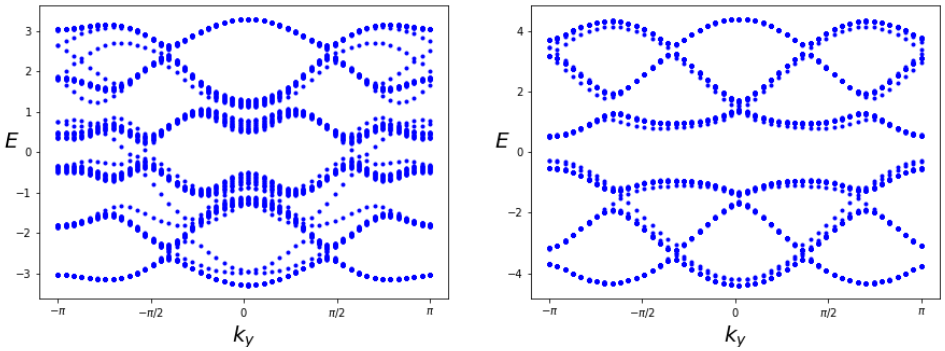

Figure 12: Energy spectrum for different λ_x with maximal spin mixing. Lattice: 48×48

structure. With the local Chern marker (3.1) we are able to assign a local Chern number to our system in real-space. For our current Hamiltonian we have to extend our derivation of the Chern number to a spin related Chern number according to [38, 39]. The Chern number of the whole Hamiltonian is zero, due to its time-reversal symmetry. However, the Chern numbers separately evaluated over spin up and spin down wavefunctions,

$$C_\sigma = -\frac{1}{\pi}\mathrm{Im}\sum_{n=1}^{N_c}\int_{BZ}\mathrm{d}\mathbf{k}\left\langle\frac{\partial u_{n\mathbf{k}\sigma}}{\partial k_x}|\frac{\partial u_{n\mathbf{k}\sigma}}{\partial k_y}\right\rangle \qquad \sigma =\uparrow,\downarrow, \tag{4.4}$$

are not always zero, since the spin decoupled parts of the Hamiltonian are not time-reversal invariant. But since

$$C = C_\uparrow + C_\downarrow = 0, \tag{4.5}$$

it is useful two define a total spin Chern number C_S for a spin decoupled Hamiltonian as

$$C_S = \frac{1}{2}(C_\uparrow - C_\downarrow), \tag{4.6}$$

where its parity is equal to the $\mathbb{Z}_2$ invariant. In the further section we will call it simply Chern number, but to be accurate it will be the spin Chern number, since we calculating a system with spin.

Our Hamiltonian is of course decoupled for $\gamma = 0$, since there is no mixing of spin up and down. The other interesting case we are looking at is $\gamma = 0.25$ or maximal spin mixing. Here we have to decouple our Hamiltonian first so that we can use equation (4.4). Looking only on the spin mixing term of (4.3) we find

$$e^{2\pi i\cdot 0.25\sigma_x} = i\sigma_x \tag{4.7}$$

The spin mixing term in our Hamiltonian (4.3) means that hopping in x-direction will flip the spin of the particle. The idea is now to describe the system in a pseudo spin basis where this information is already included in the basis vectors. For this reason we introduce the pseudo spin annihilation operators:

$$\hat{d}_{x,y,\sigma} = \begin{cases}\hat{c}_{x,y,\sigma} & \text{if } x \text{ is even}\\ \hat{c}_{x,y,\bar{\sigma}} & \text{if } x \text{ is odd}\end{cases} \tag{4.8}$$

The transformation from one to the other basis is given by

$$\hat{d}_{x,y} = (\sigma_x)^x\hat{c}_{x,y} \tag{4.9}$$

$$\hat{d}^\dagger_{x,y} = \hat{c}^\dagger_{x,y}(\sigma_x)^x, \tag{4.10}$$

where σ_x is a Pauli matrix and $\sigma_x^2 = \mathbb{1}$. We now have to look at the terms of the Hamiltonian (4.3) to see if the transformation really decouples it. We find

$$\hat{c}^\dagger_j\hat{c}_j = \hat{d}^\dagger_j(\sigma_x)^{2x}\hat{d}_j = \hat{d}^\dagger_j\hat{d}_j, \tag{4.11}$$

$$\hat{c}^\dagger_{j+\hat{x}}i\sigma_x\hat{c}_j = \hat{d}^\dagger_{j+\hat{x}}(\sigma_x)^{x+1}i\sigma_x(\sigma_x)^x\hat{d}_j = i\cdot\hat{d}^\dagger_{j+\hat{x}}\hat{d}_j, \tag{4.12}$$

$$\hat{c}^\dagger_{j+\hat{y}}e^{2\pi ix\sigma_z\alpha}\hat{c}_j = \hat{d}^\dagger_{j+\hat{y}}(\sigma_x)^x e^{2\pi ix\sigma_z\alpha}(\sigma_x)^x\hat{d}_j = \hat{d}^\dagger_{j+\hat{y}}e^{(-1)^x 2\pi ix\sigma_z\alpha}\hat{d}_j, \tag{4.13}$$

and therefore the whole Hamiltonian reads:

$$\hat{H}_d = -t \sum_j \left[\left(\hat{d}^\dagger_{j+\hat{x}} e^{i\pi/2} \hat{d}_j + \hat{d}^\dagger_{j+\hat{y}} e^{(-1)^x 2\pi i x \sigma_z \alpha} \hat{d}_j + h.c. \right) + (-1)^x \lambda_x \hat{d}^\dagger_j \hat{d}_j \right]. \tag{4.14}$$

Our result only depends on σ_z matrices, therefore not mixing pseudo spin up and pseudo spin down. Furthermore we get a staggered plaquette flux $\alpha \to (-1)^x \alpha$ for hopping in y-direction. The pseudo spin basis has no direct physical meaning, but we can now evaluate the local Chern number for the decoupled parts of the Hamiltonian with equation (4.4) and combine them to a total spin Chern number according to equation (4.6). To get a better feeling for the local Chern marker we first look at its local distribution on the lattice at half filling and maximal spin mixing plotted in figure 13. The local Chern marker is everywhere zero in regimes where the

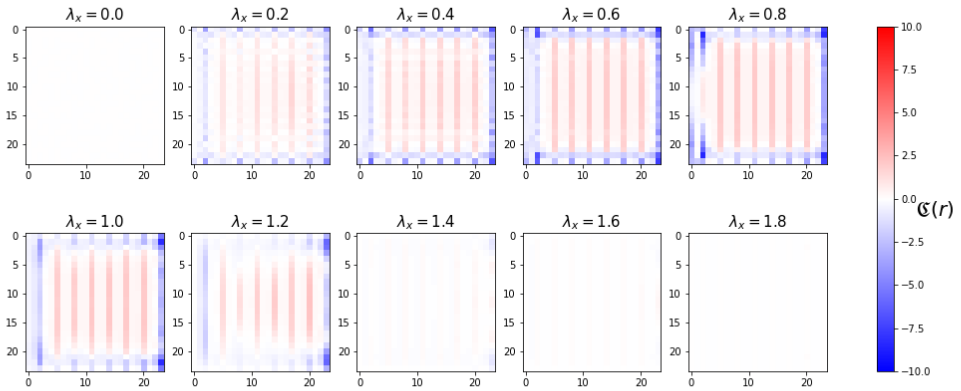

Figure 13: Local distribution of the Chern marker on the lattice for different λ_x. Lattice: 24×24, $\gamma = 0.25$, $E_F = 0$.

system is in a normal insulating phase. In the QSH regime the local Chern number has values of around 1 in the bulk, but strongly divergent values at the edges. This behavior explains the idea of cutting of the edges and averaging about the bulk to obtain the Chern number of the system. The transformation yields a staggered plaquette flux, while hopping in y-direction, which is the reason for the stripes in figure 13. The stripes appearing periodically every third lattice site. One can see this by explicitly calclulating the picked up phase for hopping around a plaquette. For example hopping around one plaquette along lattice sites in the following way (figure 14):

$$(x, y) \to (x + 1, y) \to (x + 1, y + 1) \to (x, y + 1) \to (x, y), \tag{4.15}$$

Without spin mixing the picked up phase Φ was

$$\Phi = 2\pi\alpha, \tag{4.16}$$

where Φ is the magnetic flux through the plaquette. Now we get a complex phase of

$$\Phi = -(-1)^x 2\pi\alpha(2x + 1) = -(-1)^x \left(\frac{2\pi x}{3} + \frac{\pi}{3} \right), \tag{4.17}$$

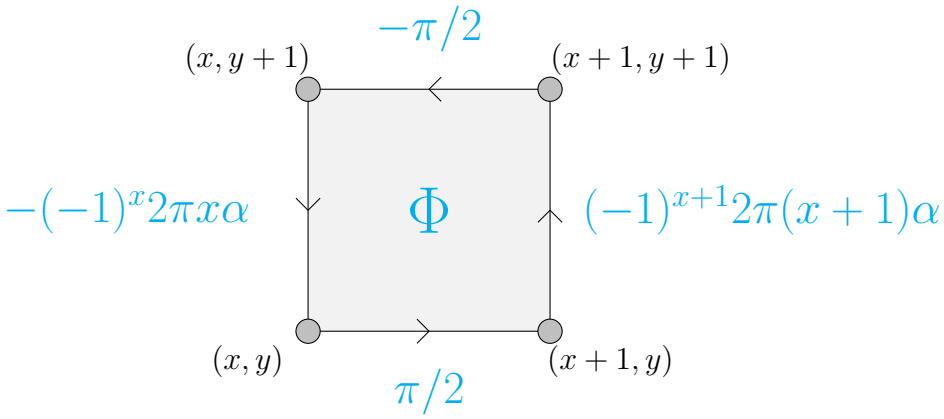

Figure 14: Hopping around one plaquette of the decoupled Hamiltonian.

which is depending on x. Here we already see the periodicity of the phase, where the number of lattice sites for one period is due to the chosen $\alpha = 1/6$. The picked up phase for every first and fourth plaquette in x-direction to a modulo of 2π, differs only by the sign, while it is equal to the phase for the seventh plaquette.

Figure 15 shows the average of the local Chern number for maximal spin mixing at half-filling within PBC. We averaged over the bulk, but for different cut-offs. For example a cut-off of one means the local Chern number is averaged over the lattice, but without the first and last of the rows and columns. The thin blue line describes the size of the gap as we have seen before in

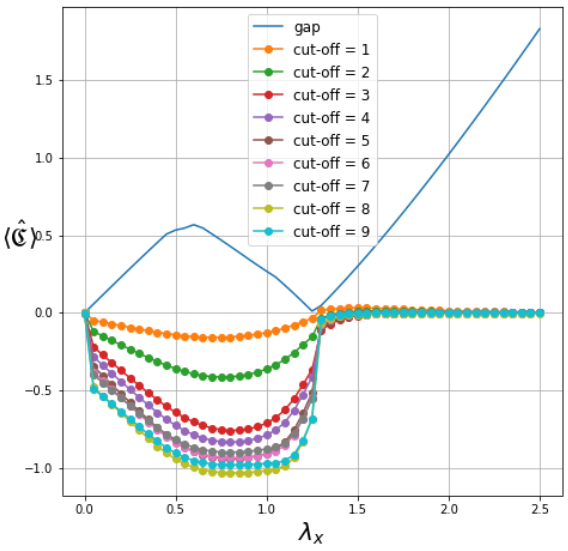

Figure 15: The blue line shows the size of the gap according to figure 11, the dotted lines are the values of the local Chern marker averaged over the lattice with different cut-offs. Lattice: 24×24, $E_F = 0$, $\gamma = 0.25$.

figure 11. It is a property of the local Chern number to be zero when averaged over the whole sample. If we want to calculate the local Chern number only for the bulk region of the lattice,

where the Chern number becomes more accurate, we have to go to a greater cut-off. As the gap opens we should see a QSH phase with a Chern number going to -1 or 1. As we see in figure 15 the accuracy is also higher for a larger gap. After the gap closes the system is in a NI phase as the Chern number is zero. The cut-off is of course limited by the system size. We used a 24×24 lattice, which means a cut-off of nine at both sides already results in a very small lattice. The difference between the local Chern marker on the left and right side of the gap maximum are also due to finite size effects. We are now able to calculate the whole phase diagram for different boundary conditions. We first start with no spin mixing i.e. $\gamma = 0$. The black lines in figure 16

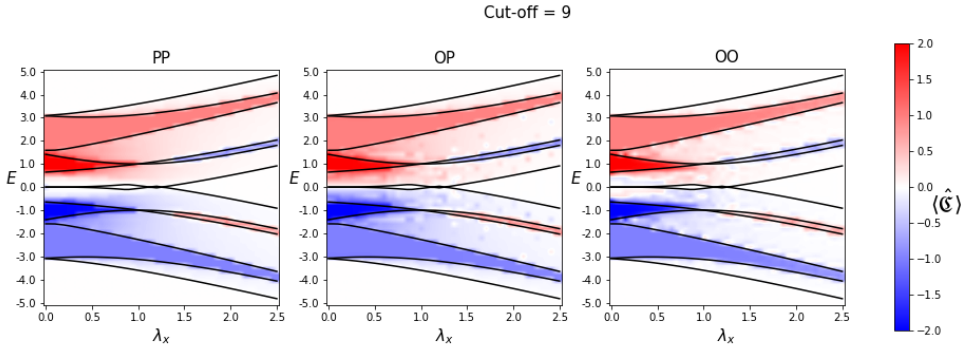

Figure 16: Phase diagram of the local Chern number for no spin mixing and different boundary conditions (P stands for PBC, O stands for OPC in x- respectively y-direction). Lattice: 24×24, $\gamma = 0.0$.

are the bounds of the metal regime obtained from the system with PBC and can be used for orientation. Between two black lines there should either be a metallic phase or a gap. White color means the system is in a metallic or NI phase. The colored regimes fit well between the black lines, even if they are a little bit blurred over the bounds, and the obtained value for the local Chern number is accurate. The Chern number in the regime around $\mu = \pm 2.5$ is about ± 1 and the system is therefore in a QSH phase. We obtained this before for $\lambda_x = 0$ in the energy spectrum by counting the number of Kramers pairs in figure 9. Within the gap around $\mu = \pm 1$ the system is in a NI phase due to the even Chern number. For increasing λ_x this gaps closes, opens again and is now in a QSH phase. Again the gap has to be closed to change the Chern number. Now we want to look at the phase diagram with maximal spin mixing i.e. $\gamma = 0.25$. The most interesting regime in this phase diagram (figure 17) is the QSH phase at half filling. It is induced by the spin-orbit coupling, since there is no such regime in figure 16. On half filling there are as much sites populated as free. This makes it especially interesting if one wants to bring in interactions. In the lowest gap for example, there are so few sites populated, that the propability for particles to interact is low, while in the highest gap so many sites are occupied that Pauli blocking surpresses interactions. Apart from the regime at half filling, there are two other interesting regimes at $\mu = \pm 1$. The gap is opened for $\lambda_x = 0$ and the system is in a NI phase. While increasing λ_x the gap will be closed and opens again where the system is now in a QSH phase. In figure 18 we look at the phase diagram of a larger lattice to discuss some finite size effects. The system size has 48 sites in each direction with OBC. Here the colored regions are less blurred. The reason for this is that we can take the same cut-off as in the smaller lattice, since the penetratrion depth of the edge states is not depending on the lattice size, and therefore have a larger region in the middle of the lattice, where the local Chern marker could be averaged over.

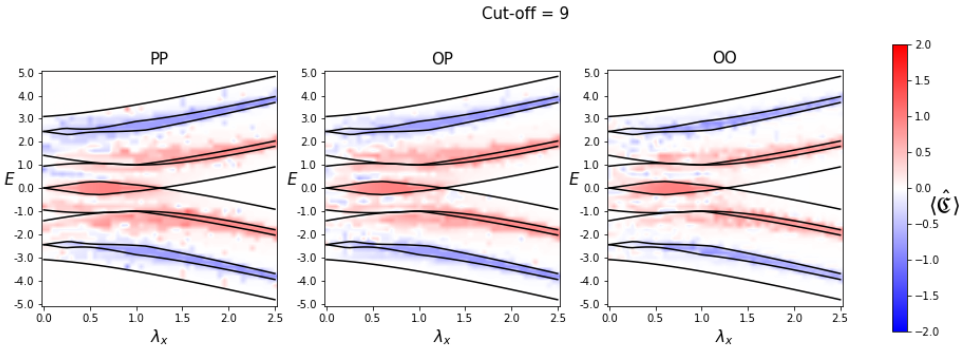

Figure 17: Phase diagram of the local Chern number for maximal spin mixing and different boundary conditions. Lattice: 24×24, $\gamma = 0.25$.

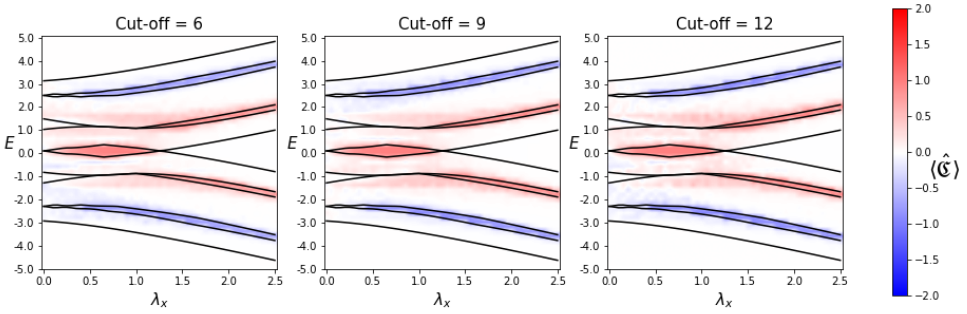

Figure 18: Phase diagram of the local Chern number for maximal spin mixing, OBC and different cut-offs. Lattice: 48×48; $\gamma = 0.25$.

The local Chern number should be equal to the integer Chern invariant for a infinite great lattice and therefore it is interesting to look how well these two quantities are matching in our calculation. In figure 19 are only the regions colored, which have a value of $|\langle\hat{\mathfrak{C}}\rangle| = 1 \pm \delta$, for

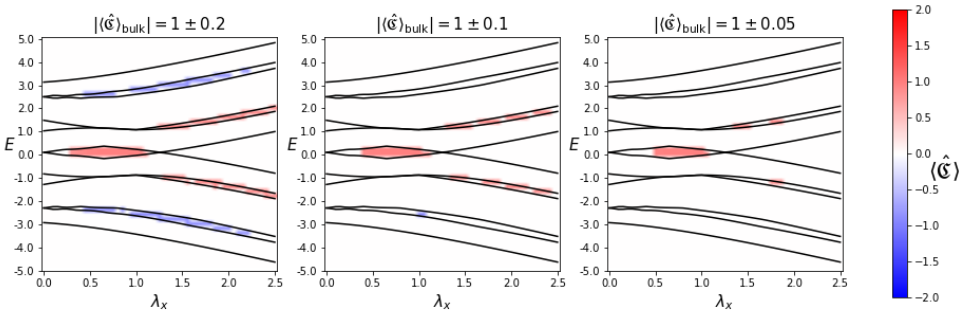

Figure 19: Accuracy of the phase diagram of the local Chern number for maximal spin mixing and OBC. Only the regions are colored where the local Chern number is within the tolerance. Lattice: 48×48, $\gamma = 0.25$.

several δ, and we see that we have got an accuracy of 10 to 20 percent in the regions with a smaller gap.
Another tool to obtain the Chern number of a system in real space is the Bott index [31]. The equivalence of the Bott index and the Chern number on a torus is shown by Tonilio [40]. Like for the local Chern marker we plotted in figure 20 the Bott index in comparison to the gap at half filling and maximal spin mixing. The Bott index is supposed to work well for gapped

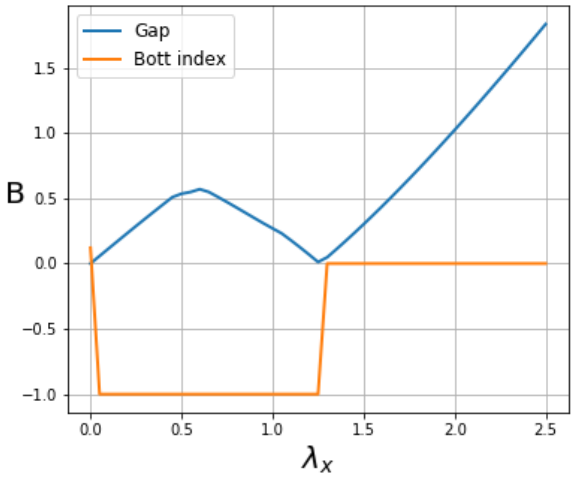

Figure 20: Bott index and gap according to figure 11 at half filling. $\gamma = 0.25, E_F = 0$.

systems and seems to be very accurate even for a small gap. So if we now calculate the phase diagram we should only calculate the Bott index in regimes where the system is gapped. The phase diagram plotted in figure 21 seems to be accurate in the gapped regimes, but looks very speckled in the metal regimes, for periodic and open-periodic boundary conditions. The specks are due to the finite size system, were there are finite gaps between the energy bands even in

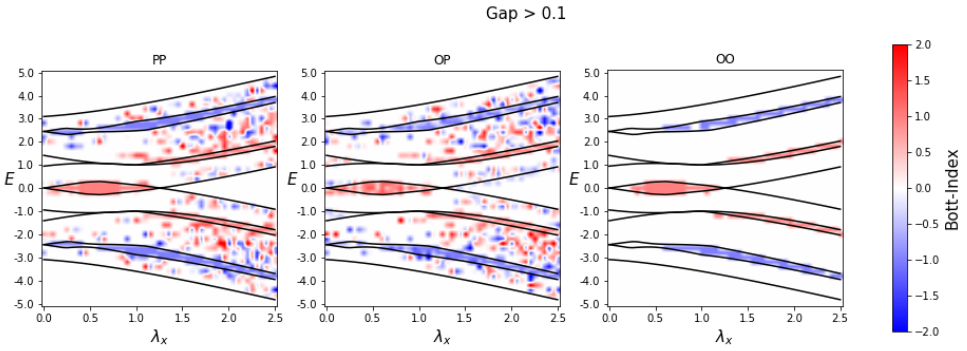

Figure 21: Phase diagram with Bott index for maximal spin mixing. Lattice: 24×24, $\gamma = 0.25$

the metal regimes. Remarkably well is the phase diagram of the non periodic system. Here it seems that the Bott index is accurate even in the metal regimes. We get the same picture for OBC even if we do not require any finite gap.

4.2 Fermions in a Trap

In an experimental setup cold atoms have to be trapped to prevent the atomic cloud from expanding in all directions. Because of this we want to calculate the local Chern marker in such more realistic systems. We are going to discuss three different trap geometries; the hard wall, the harmonic and the quartic trap. For simplicity the trap potential will just change in x-direction and the system will be periodic in y-direction. The Hamiltonian now reads

$$\hat{H} = -t \sum_j \left[\left(\hat{c}^\dagger_{j+\hat{x}} e^{-2\pi i \gamma \sigma_x} \hat{c}_j + \hat{c}^\dagger_{j+\hat{y}} e^{i 2\pi \alpha x \sigma_z} \hat{c}_j + h.c. \right) + (-1)^x \lambda_x \hat{c}^\dagger_j \hat{c}_j + V(x) \hat{c}^\dagger_j \hat{c}_j \right], \qquad (4.18)$$

with a trap potential $V(x)$,

hard wall	harmonic trap	quartic trap
$V(x) = \begin{cases} 0 & \text{for } 0 < x \leq N \\ \infty & \text{else} \end{cases}$	$V(x) = (x - \frac{N+1}{2})^2$	$V(x) = (x - \frac{N+1}{2})^4$
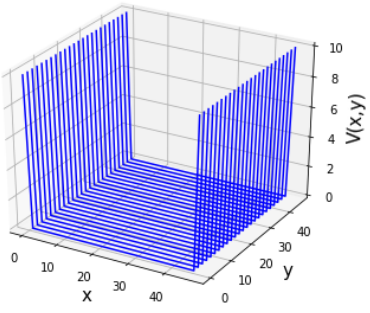	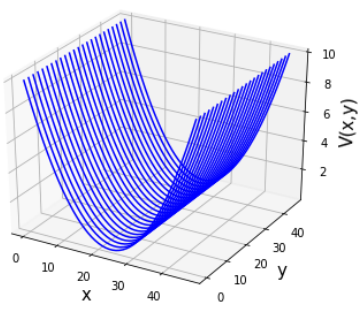	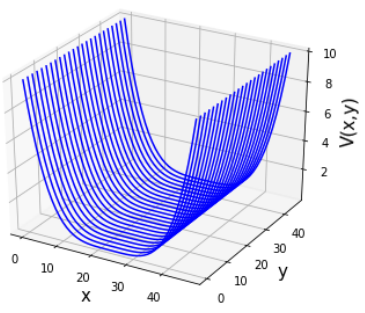

where N is the number of lattice sites in x-direction. These geometries have been studied before by Buchold et al.[35] for spinless fermions and therefore $\gamma = 0$. We are going to discuss which new insights the method of the local Chern marker brings in a system with spinful fermions and study systems with maximum spin mixing ($\gamma = 0.25$).

Since the system is periodic in y-direction the quasi momentum k_y and position operator x are well defined. Therefore one could plot the energy spectra with respect to both quantities. We use the spectral density defined as

$$\rho_x^\sigma(k_y, E) = -2\mathrm{Im}\left\langle x, k_y, \sigma\right| \frac{1}{E - H(k_y, x, \sigma) + i0^+} \left|x, k_y, \sigma\right\rangle, \tag{4.19}$$

to calculate them. Here σ denotes the spin we are looking at. One could obtain the momentum-energy spectrum by summing the spectral density over all sites in x-direction

$$\rho^\sigma(k_y, E) = \sum_{x=0}^{N} \rho_x^\sigma(k_y, E). \tag{4.20}$$

In the same way the momentum-integrated spectral density yields the real-space spectrum

$$\rho_x^\sigma(E) = \int \mathrm{d}k_y \rho_x^\sigma(k_y, E). \tag{4.21}$$

For a spin-decoupled Hamiltonian one has to sum over both spins to get the whole spectrum

$$\rho = \rho^\uparrow + \rho^\downarrow. \tag{4.22}$$

On the other hand we calculate the local Chern marker $\mathfrak{C}(\mathbf{r})$ (3.35) for a chosen energy, up to which all bands are occupied. Figure 22 shows the results for system with quartic confinement

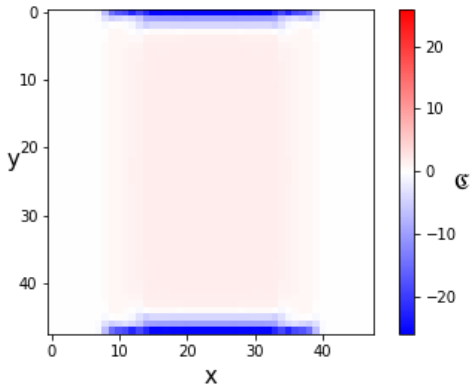

Figure 22: Local Chern marker for a periodic system in y-direction with quartic confinement in x-direction. $E = -1.0$; Lattice: 48×48.

and which is filled up to an energy of $E = -1.0$. The confinement prohibits the particles to extend to the boundaries in x-direction, therefore the local Chern marker there is zero and there aren't boundary effects like in y-direction, where the system is periodic. To get rid of those boundary effects we have to cut off the edges. Now we can average about the remaining lattice sites in y-direction to get a x-dependent local Chern marker

$$\mathfrak{C}(x) = \frac{1}{M - 2 \cdot m_{cut}} \sum_{y=m_{cut}}^{M-m_{cut}} \mathfrak{C}(x, y), \tag{4.23}$$

where M is the number of lattice sites in y-direction and m_{cut} is the number of lattice sites, which are cut off at both edges. For further calculations we set $m_{cut} = 12$ for a lattice size of

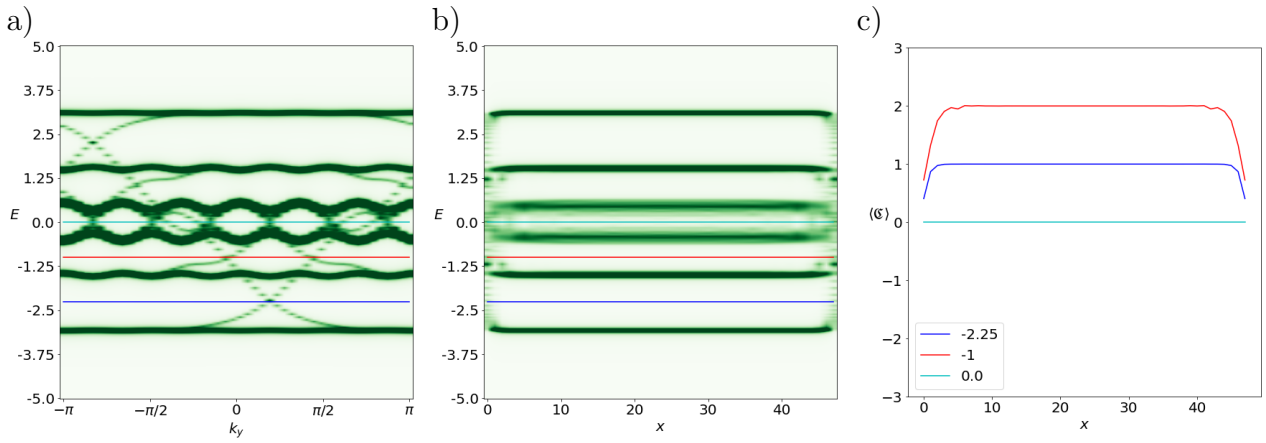

Figure 23: Momentum- (a), real-space (b) spectra and local Chern marker (c) for several energies in hard wall confinement. The momentum-energy spectrum contains only one spin. Lattice: 48×48; $\lambda_x = 0$; $\gamma = 0$.

48×48.

We start without spin mixing and staggered potential ($\gamma = \lambda_x = 0$). The following momentum-energy spectra in figure 23-25 include just one spin, so that they are clearer to read. In figure 23 one can see the already discussed momentum-energy spectrum as well as the real-space spectrum for a system in hard wall confinement. In the real-space spectrum we can see the flat occupied bands and the gaps, where we have a finite density of states only at the edges. We calculated the local Chern marker according to equation (4.23) for several energies corresponding to the colored lines. It has a wide flat plateau in the middle of the lattice, corresponding to whether it is in a QSH or NI phase. We already got this information, since we calculated the whole phase diagram for a system with hard wall boundaries (figure 17). New is now the spatial behaviour of the local Chern marker, which drops towards zero at the edges. The topology outside the trap has to be zero since there are no states allowed. This spatial behaviour is even more interesting if we look at systems with smooth confinement. In figure 24 we see the energy spectra of a system within a quartic trap. While the momentum-energy spectrum is very crowded and it is hard to distinguish between bulk and edge modes, this is clearer in the real-space spectrum. The flat regions in the middle correspond to bulk bands, while the edge states are at the sides. In the right picture in figure 24 there is the local Chern marker plotted and below the qualitative behaviour of the spectral density $\rho_x(E)$. Following the blue line there are two peaks around lattice sites 11 and 36. Besides and between them the spectral density is zero. One can see that the local Chern marker changes its value from zero to one and later back at the sites where the spectral density peaks. In other words we see two regions of different topology, which are connected by an edge state. Since we are describing spinful fermions, such a peak in the spectral density does not correspond to a single edge state but to a Kramer's pair of counterpropagating states and we see here a nice confirmation of the bulk-boundary correspondence. Looking at the spectral density along the red line in figure 24 one finds two big peaks at each side. Around the first, the local Chern marker rises to one, while after the second peak it has a value of two which indicates a normal insulating phase. This also suits the statement of the bulk-boundary correspondence, where two Kramer's pairs on one side correspond two a $\mathbb{Z}_2$ index of zero and therefore a trivial phase. In the paper by Buchold at al.[35] the $\mathbb{Z}_2$ index was obtained by

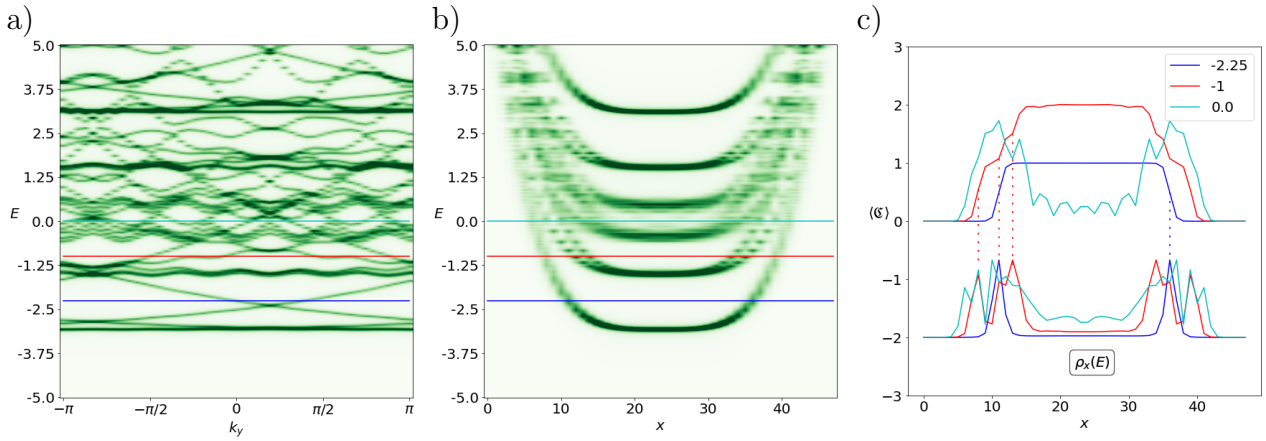

Figure 24: Momentum- (a), real-space (b) spectra and local Chern marker (c) for several energies in quartic confinement. The momentum-energy spectrum contains only one spin. The lower curves in the right picture are the qualitative behaviour of the spectral density $\rho_x(E)$. Lattice: 48×48; $\lambda_x = 0$; $\gamma = 0$.

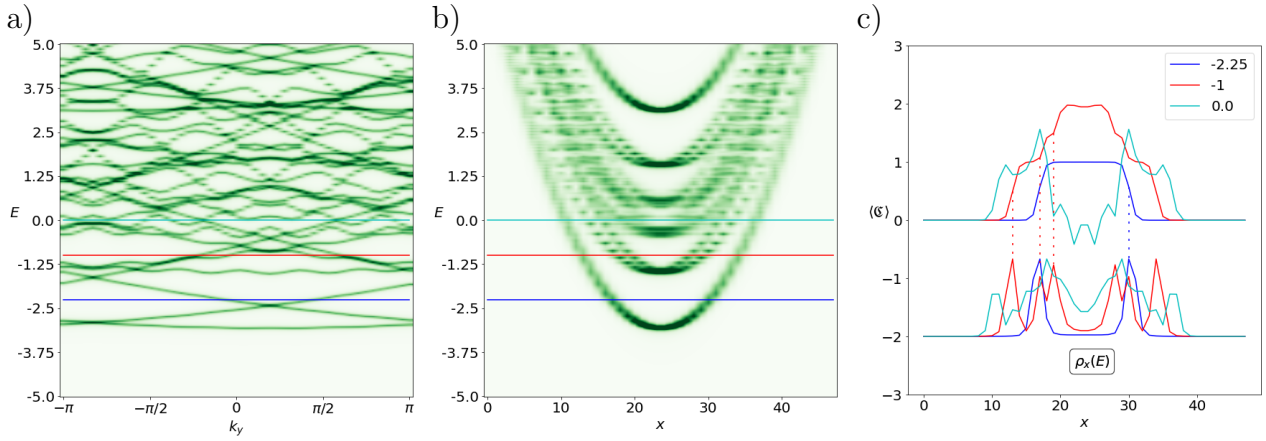

Figure 25: Momentum- (a), real-space (b) spectra and local Chern marker (c) for several energies in harmonic confinement.The momentum-energy spectrum contains only one spin. The lower curves in the right picture are the qualitative behaviour of the spectral density $\rho_x(E)$. Lattice: 48×48; $\lambda_x = 0$; $\gamma = 0$.

defining the edge as the point at which no states have energies within the range of energies covered by states at the center of the trap. This means all bulk states are having the same energies within a small range. In a system with harmonic confinement shown in figure 25 this definiton leads to such a small bulk region, that it contradicts the concept of a bulk. If we look at the momentum-energy spectrum it is also not possible to distinguish between edge and bulk states. The advantage of the local Chern marker is that it does not require any definition of bulk and edge. In figure 25 we have qualitative similar results for the local Chern marker as in quartic confinement, with the edge states just closer to the center of the trap. Also the changes in the local Chern marker could be associated with peaks in the spectral density. In figure 26

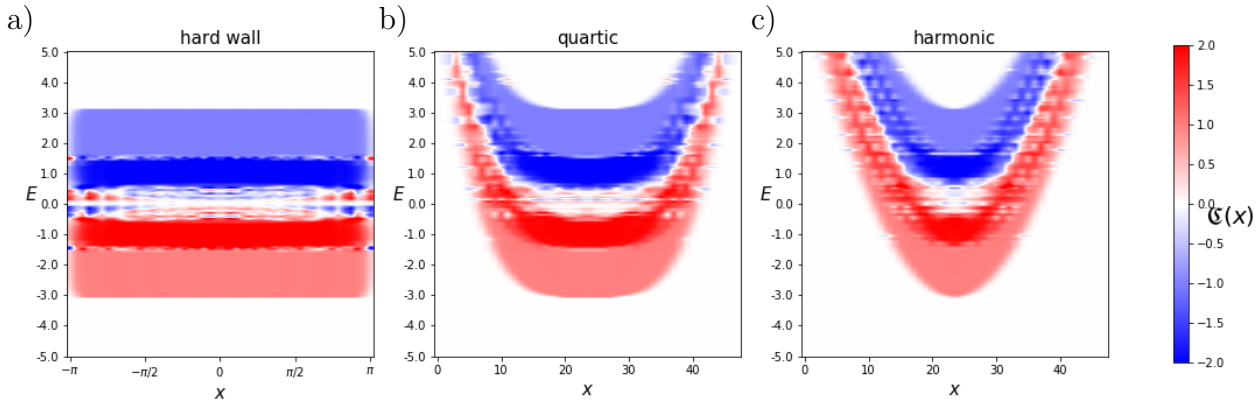

Figure 26: Spatial behaviour of the local Chern marker $\mathfrak{C}(x)$ for the whole energy spectrum and different traps. Lattice: 48×48; $\lambda_x = 0$; $\gamma = 0$.

the local Chern marker $\mathfrak{C}(x)$ is plotted for all energies in the spectrum. So every horizontal line corresponds to its spatial behaviour in x-direction for one energy, while the values of $\mathfrak{C}(x)$ are associated with the color. The different phases are good to distinguish and one can see for which energies interesting QSH phases appear and how big such regions are.
Now we want to turn on spin orbit coupling and therefore set $\gamma = 0.25$. From the phase diagram in figure 18 we know that there is a QSH regime opening at half filling if we increase λ_x. The gap there has its maximum size around $\lambda_x = 0.5$ so we choose this value for our calculations. By

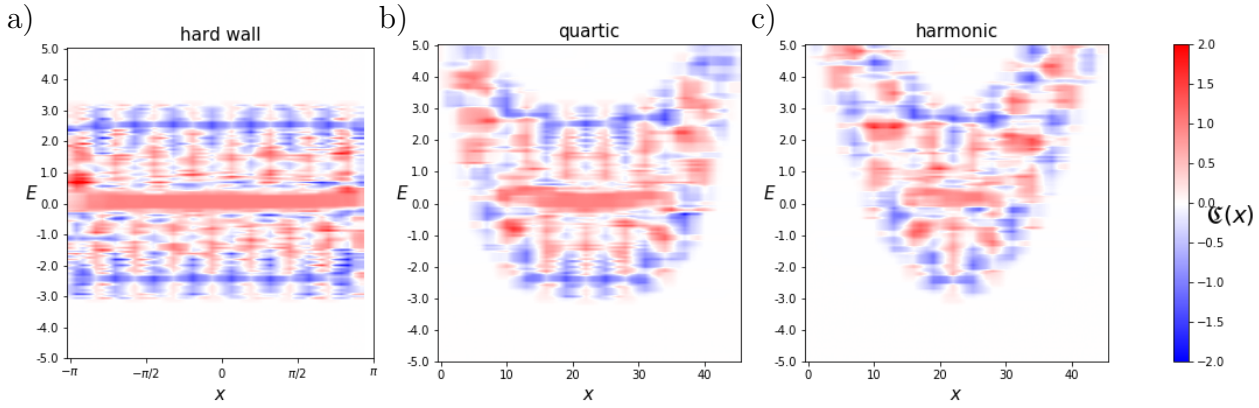

Figure 27: Spatial behaviour of the local Chern marker $\mathfrak{C}(x)$ for the whole energy spectrum with maximum spin mixing. Lattice: 48×48; $\lambda_x = 0.5$; $\gamma = 0.25$.

looking at the distribution of the local Chern marker plotted in figure 27 one can see that this

QSH regime at half filling is also appearing in systems with quartic and harmonic confinement. Since there are no other interesting areas we will focus on energies around half filling. We discussed before the stripes in figure 13, which emerge if we induce spin-orbit coupling. In these figures (27, 28, 29) the value of the local Chern marker is averaged about three lattice sites in x-direction to surpress these oscillations and get smooth curves.

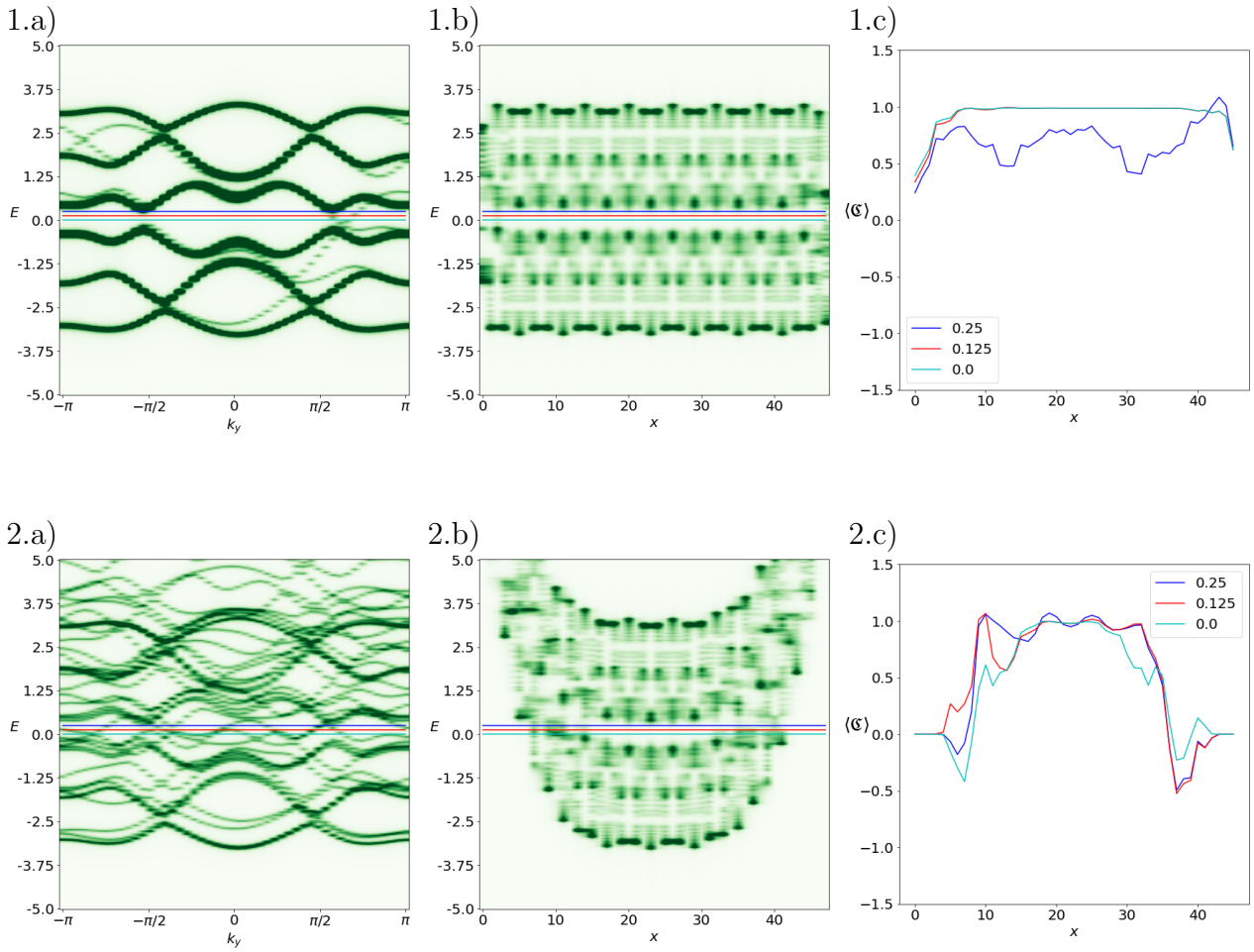

Figure 28: Momentum- (a), real-space (b) spectra and local Chern marker (c) for several energies in hard wall (1)and quartic (2) confinement. The momentum-energy spectrum contains only one spin. Lattice: 48×48; $\lambda_x = 0.5$; $\gamma = 0.25$.

The results are plotted in figure 28 for all three traps. For the cases of hard wall and quartic confinement the local Chern marker has a flat plateau indicating a QSH phase in the center of the trap. In harmonic confinement it tends to one, but not really reaches a plateau, and varies greatly by slightly changing the energy. All results were calculated for a 48×48 square lattice. The actually occupied lattice in the harmonic confinement has around half the size, therefore finite size effects may distort the result.

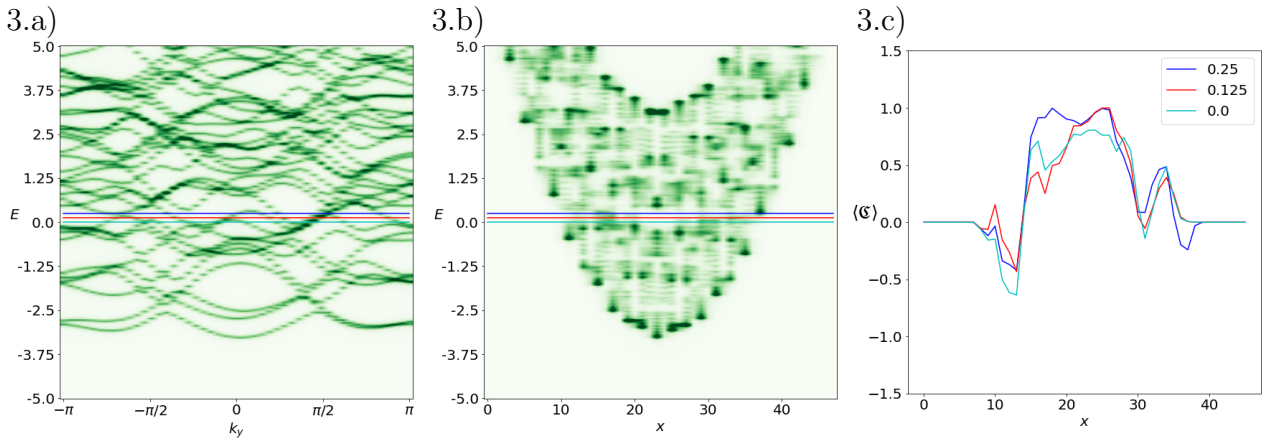

Figure 29: Momentum- (a), real-space (b) spectra and local Chern marker (c) for several energies in harmonic (3) confinement. The momentum-energy spectrum contains only one spin. Lattice: 48×48; $\lambda_x = 0.5$; $\gamma = 0.25$.

5 Discussion

In this thesis we disussed the time-reversal invariant Harper-Hofstadter Hamiltonian, to describe noninteracting spinful fermions in a square lattice with an external magnetic field perpendicular to it. We saw the emergence of the topological quantum spin Hall phase and obtained the $\mathbb{Z}_2$-index from the momentum-energy spectrum in a system with OBC according to the bulk-boundary correspondence. Afterwards we discussed the concept of a Chern number and mapped this topological invariant from momentum-space to real-space using the local Chern marker. With this method we were now able to calculate the $\mathbb{Z}_2$-index for systems independently of the boundary conditions. We added a staggered potential to the Hamiltonian to drive phase transitions and calculated phase diagrams for increasing staggered potential. For the case of a system with maximum spin-orbit coupling, which couples the spins in the Hamiltonian we introduced a transformation to decouple the Hamiltonian and also calculated the phase diagram using the local Chern marker. We showed that the phase diagrams in both cases are independent of the choice of boundary conditions, which confirms that the topology of a system is an attribute of the bulk. Edge states are an effect of finite or inhomogenous systems to connect regions of different topology. We checked our results with the bott index, which yields qualitatively similar results. The local Chern marker shows its strengths especially in inhomogenous systems, where it could give spatially resolved results. Therefore we considered three different trap geometries, which we implemented in the Hamiltonian: hard wall, harmonic or quartic trap in one direction, while the other is periodic. The local Chern marker shows QSH regimes in all trap geometries. We compared the distribution of the local Chern marker to the real-space energy spectra of the systems obtained by the spectral function. There we saw that the appearance of an edge state is correlated with a change in the local Chern marker, which is a nice confirmation of the bulk-boundary correspondence. In systems with maximum spin-orbit coupling, there is a QSH regime at half filling in all three trap geometries. This is interesting for further studies on interacting fermions, since interactions have the strongest impact at half filling.

References

[1] K. B. Davis, M. O. Mewes, M. R. Andrews, N. J. van Druten, D. S. Durfee, D. M. Kurn, and W. Ketterle. Bose-einstein condensation in a gas of sodium atoms. *Phys. Rev. Lett.*, **75**:3969, (1995).

[2] M. H. Anderson, J. R. Ensher, M. R. Matthews, C. E. Wieman, and E. A. Cornell. Observation of bose-einstein condensation in a dilute atomic vapor. *Science*, **269**:198, 1995.

[3] M. R. Inouye, S.and Andrews, J. Stenger, H. J. Miesner, D.M. Stamper-Kurn, and W. Ketterle. Observation of feshbach resonances in a bose-einstein condensate. *Nature*, **392**:151, (1998).

[4] T. Bourdel, L. Khaykovich, J. Cubizolles, J. Zhang, F. Chevy, M. Teichmann, L. Tarruell, S. J. J. M. F. Kokkelmans, and C. Salomon. Experimental study of the bec-bcs crossover region in lithium 6. *Phys. Rev. Lett.*, **93**:050401, (2004).

[5] M. Greiner and S. FÃ¶lling. Optical lattices. *Nature*, **453**:736, (2008).

[6] Markus Greiner, Olaf Mandel, Tilman Esslinger, Theodor W. Hänsch, and Immanuel Bloch. Quantum phase transition from a superfluid to a mott insulator in a gas of ultracold atoms. *Nature*, **415**:39, (2002).

[7] M. J. Mark, E. Haller, K. Lauber, J. G. Danzl, A. J. Daley, and H.-C. Nägerl. Precision measurements on a tunable mott insulator of ultracold atoms. *Phys. Rev. Lett.*, **107**:175301, (2011).

[8] K. W. Madison, F. Chevy, W. Wohlleben, and J. Dalibard. Vortex formation in a stirred bose-einstein condensate. *Phys. Rev. Lett.*, **84**:806, (2000).

[9] Wilhelm Zwerger. Mott-hubbard transition of cold atoms in optical lattices. *J. Opt. B-Quantum S. O.*, **5**:S9, (2003).

[10] Hirokazu Miyake, Georgios A. Siviloglou, Colin J. Kennedy, William Cody Burton, and Wolfgang Ketterle. Realizing the harper hamiltonian with laser-assisted tunneling in optical lattices. *Phys. Rev. Lett.*, **111**:185302, (2013).

[11] M. Aidelsburger, M. Atala, M. Lohse, J. T. Barreiro, B. Paredes, and I. Bloch. Realization of the hofstadter hamiltonian with ultracold atoms in optical lattices. *Phys. Rev. Lett.*, **111**:185301, (2013).

[12] Y.-J. Lin, K. Jiménez-García, and I. B. Spielman. Spin-orbit-coupled bose-einstein condensates. *Nature*, **471**:83, (2011).

[13] M. Endres, M. Cheneau, T. Fukuhara, C. Weitenberg, P. Schauß, C. Gross, L. Mazza, M. C. Bañuls, L. Pollet, I. Bloch, and S. Kuhr. Single-site- and single-atom-resolved measurement of correlation functions. *Appl. Phys. B-Lasers O*, **113**:27, (2013).

[14] Immanuel Bloch, Jean Dalibard, and Wilhelm Zwerger. Many-body physics with ultracold gases. *Rev. Mod. Phys.*, **80**:885, (2008).

[15] K. v. Klitzing, G. Dorda, and M. Pepper. New method for high-accuracy determination of the fine-structure constant based on quantized hall resistance. *Phys. Rev. Lett.*, **45**:494, (1980).

[16] R. B. Laughlin. Quantized hall conductivity in two dimensions. *Phys. Rev. B*, **23**:5632, (1981).

[17] D. J. Thouless, M. Kohmoto, M. P. Nightingale, and M. den Nijs. Quantized hall conductance in a two-dimensional periodic potential. *Phys. Rev. Lett.*, **49**:405, (1982).

[18] C. L. Kane and E. J. Mele. Quantum spin hall effect in graphene. *Phys. Rev. Lett.*, **95**:226801, (2005).

[19] B. Andrei Bernevig and Shou-Cheng Zhang. Quantum spin hall effect. *Phys. Rev. Lett.*, **96**:106802, (2006).

[20] Naoto Nagaosa. A new state of quantum matter. *Science*, **318**:758, (2007).

[21] Markus König, Steffen Wiedmann, Christoph Brüne, Andreas Roth, Hartmut Buhmann, Laurens W. Molenkamp, Xiao-Liang Qi, and Shou-Cheng Zhang. Quantum spin hall insulator state in hgte quantum wells. *Science*, **318**:766, (2007).

[22] Colin J. Kennedy, Georgios A. Siviloglou, Hirokazu Miyake, William Cody Burton, and Wolfgang Ketterle. Spin-orbit coupling and quantum spin hall effect for neutral atoms without spin flips. *Phys. Rev. Lett.*, **111**:225301, (2013).

[23] Y. Aharonov and D. Bohm. Significance of electromagnetic potentials in the quantum theory. *Phys. Rev.*, **115**:485, (1959).

[24] Ambrož Kregar. Seminar - 4. letnik; aharonov-bohm effect. University of Ljubljana, Faculty of Mathematics and Physics, Ljubljana, marec 2011.

[25] R. Peierls. Zur theorie des diamagnetismus von leitungselektronen. *Z. Phys.*, **80**:763, (1933).

[26] J. J. Sakurai. *Modern Quantum Mechanics*. Pearson, (1993).

[27] J. K. Asbóth, L. Oroszlány, and A. Pályi. A Short Course on Topological Insulators: Band-Structure Topology and Edge States in One and Two Dimensions. *ArXiv e-prints*, September (2015).

[28] Raffaello Bianco and Raffaele Resta. Mapping topological order in coordinate space. *Phys. Rev. B*, **84**:241106, (2011).

[29] D.-T. Tran, A. Dauphin, N. Goldman, and P. Gaspard. Topological Hofstadter Insulators in a Two-Dimensional Quasicrystal. *Phys. Rev. B*, **91**:085125, (2015).

[30] Stefano Baroni, Stefano de Gironcoli, Andrea Dal Corso, and Paolo Giannozzi. Phonons and related crystal properties from density-functional perturbation theory. *Rev. Mod. Phys.*, **73**:515, (2001).

[31] T. A. Loring and M. B. Hastings. Disordered topological insulators via c* -algebras. *Europhys. Lett.*, **92**:67004, (2011).

[32] M. B. Hastings and T. A. Loring. Almost Commuting Matrices, Localized Wannier Functions, and the Quantum Hall Effect. *J. Math. Phys.*, **51**:015214, (2010).

[33] S. Eilers, T. A. Loring, and Pederson G. K. Stability of anticommutation relations: An application of noncommutative cw complexes. *J. Reine Angew. Math.*, **409**:101, (1998).

[34] Peter P. Orth, Daniel Cocks, Stephan Rachel, Michael Buchhold, Karyn Le Hur, and Walter Hofstetter. Correlated topological phases and exotic magnetism with ultracold fermions. *J. Phys. B-At. Mol. Opt.*, **46**:134004, (2013).

[35] Michael Buchhold, Daniel Cocks, and Walter Hofstetter. Effects of Smooth Boundaries on Topological Edge Modes in Optical Lattices. *Phys. Rev. A*, **85**:063614, (2012).

[36] C. L. Kane and E. J. Mele. Z_2 topological order and the quantum spin hall effect. *Phys. Rev. Lett.*, **95**:146802, (2005).

[37] A. Manchon, H. C. Koo, J. Nitta, S. M. Frolov, and R. A. Duine. New perspectives for rashba spin-orbit coupling. *Nat. Mater.*, **14**:871, (2015).

[38] D. N. Sheng, Z. Y. Weng, L. Sheng, and F. D. M. Haldane. Quantum spin-hall effect and topologically invariant chern numbers. *Phys. Rev. Lett.*, **97**:036808, (2006).

[39] D. N. Sheng, Leon Balents, and Ziqiang Wang. Phase diagram for quantum hall bilayers at $\nu = 1$. *Phys. Rev. Lett.*, **91**:116802, (2003).

[40] D. Toniolo. On the Equivalence of the Bott Index and the Chern Number on a Torus, and the Quantization of the Hall Conductivity with a Real Space Kubo Formula. *ArXiv e-prints*, (2017).